Investigation and Control
of Ultrashort Pulse Propagation
in Photonic Crystal Fibers and Fiber Lasers
in the Near Infrared Wavelength Region

Júlia Fekete

Ph.D. Dissertation

Supervisor:

Róbert Szipőcs, Ph.D.

Research Institute for Solid State Physics and Optics

of the Hungarian Academy of Sciences

Eötvös Loránd University, Faculty of Science

Physics Doctorate School

Head of the Doctorate School: Prof. Zalán Horváth

Statistical Physics, Biophysics and Physics of Quantum Systems Doctorate

Program

Program leader: Prof. Jenő Kürti

Budapest, 2009.

Contents

Introduction

Ultrafast optics have found numerous applications in the areas of fundamental research as well as of medicine and industry. Application fields include micromachining, two-photon fluorescence microscopy and optical coherence tomography, time-resolved spectroscopy in femtochemistry, optical frequency metrology, terahertz generation, etc. Most of these applications utilize femtosecond to picosecond pulses in the near infrared region (0.75 − 1.4 µm).

The most beneficial from the practical point of view would be to generate and deliver ultrashort pulses in optical fibers. Generally, ultrashort pulses change their spectral and temporal shapes during propagation in optical fibers due to the nonlinear and dispersive effects. These effects may be of orders of magnitude higher in fibers compared to bulk media, because of the long interaction length of light with matter. Under controlled circumstances, however, pulses can be transmitted over long distances in fibers with low loss and negligible distortion. On the other hand, some applications require strong nonlinearity. By their special structure, photonic crystal fibers offer greatly enhanced design freedom compared to standard optical fibers. They allow the control of the dispersion profile over a broad wavelength range, and by the adjustment of the core size and medium, nonlinearity can be varied on a wide scale, while maintaining single-mode propagation.

During my Ph.D. work, I was engaged in topics on the generation of ultrashort pulses in fiber lasers, the propagation of such pulses in photonic crystal fibers and the design of special purpose photonic crystal fibers. Some parts of these topics included theoretical work with numerical simulations. However, most of the results described in the theses are experimental, and the research was essentially motivated by practical applications. An outline and premises of the theses are described in the followings. The theses are also itemized in the Summary (Chapter 4.5).

Ultrashort pulses are originally generated by complicated setups including dye lasers exploiting colliding pulse mode-locking or solid-state lasers. Due to the advances in optical fiber technology, considerable attention is drawn by light sources that consist of fiber optical components, possibly in an all-fiber setup, for their compactness. Passively mode-locked lasers are usually operated in the anomalous dispersion regime. To overcome material dispersion of the optical elements, − i.e., the dispersion of standard silica fibers is normal below 1.3 µm, − dispersion compensation is needed in the laser cavity. Previous attempts on the realization of fiber lasers included dispersion compensation by bulk optics (e.g. gratings) or dispersion-managed optical fibers such as photonic crystal or higher-order mode fibers. In

contrast, lately it was shown that stable solutions of passively mode-locked lasers can be found in the normal dispersion regime as well, which enables the elimination of dispersion compensation in the cavity and further enhances the possible output pulse energies. Our purpose was to develop a fiber laser producing femtosecond pulses around 1 µm. During our work, we focused on the possibility of realization of an all-fiber, "all-normal dispersion" ytterbium ring oscillator [T3]. The laser operational and pulse characteristics were investigated, which may contribute to better understanding the pulse shaping mechanism of passively mode-locked fiber lasers working in the normal dispersion regime.

Compression of chirped pulses by dispersion-compensation is possible by the use of fiber integrated components. However, their use is often limited by the nonlinear interaction of the relative high peak power of pulses with the silica core. A promising route to avoid nonlinear spectral broadening in a dispersion compensating fiber, is the application of hollow-core (Bragg) photonic crystal fibers, in which most of the energy of the pulse is confined in air. It was found, however, that the silica struts in realistic hollow-core fibers, holding the space between silica layers cause a loss mechanism, called leaking modes. Our investigations on one-dimensional grazing incidence dielectric multilayer structures showed that the leaking modes can be eliminated by appropriate design of the structure. Calculations by the one-dimensional transfer matrix method used for the design of plane dielectric multilayer structures were compared to the full-vectorial finite element method that simulated the appropriate fiber structure [T1]. The qualitative agreement between the simulation results showed that the one-dimensional model is capable of giving estimates for the bandgap. It is thus an efficient complementary tool for designing Bragg photonic crystal fibers, however, it does not eliminate the need for accurate calculations by the finite element method.

Dispersion-compensation is not sufficient in compressing pulses below the Fourier transform limit. For this purpose, spectral broadening is necessary which can be realized by nonlinear phenomena in optical fibers. For relatively low peak powers, the nonlinear spectral broadening can be achieved in photonic crystal fibers with reduced core size. According to simulations of pulse propagation and optimization of dispersion-compensation coefficients, experimental demonstration of pulse compression is done on 24 fs pulses from a Ti:sapphire laser [T2].

The composition of ultrashort pulse generation, dispersion compensation and pulse compression can be introduced in the above context, but in order to follow the logic of the theoretical background, the sequence of the theses is different and

follows the concept of the Background (Chapter 1). In Chapter 1 the theory of pulse propagation in optical fibers is reviewed by deriving the basic equations for the transversal modes and the temporal behaviour in the fiber. Simulation methods for the transversal modes are described in Section 1.3, and the proposed design method of hollow-core photonic crystal fibers is further detailed based on the one-dimensional analogy in Chapter 2. Modeling of the temporal behaviour in optical fibers is done by numerically solving the so-called Nonlinear Schrödinger equation. The experiment on pulse compression is carried out based on simulations of pulse propagation in a highly nonlinear photonic crystal fiber. The results are shown in Chapter 3. Simulation of pulse propagation is also done for fiber lasers. An overview of these simulations is given in the Background chapter, to help the understanding of the complex behavior of mode-locked fiber lasers. The experimental work on the all-fiber, all-normal dispersion ytterbium ring oscillator is described in Chapter 4.

1 Background

In this chapter the basic concepts of pulse propagation in optical fibers and fiber lasers are discussed. In Section 1.1, a summary of the *Theory of pulse propagation in optical fibers* is given, based on [1]. In principle, the solution of the Helmholtz equation leads to two important equations, one of which determines the transversal mode distribution, the other one determines longitudinal propagation of pulses. Simulations on fiber modes by *The finite element method* [2, 3] and *The transfer matrix method of Bragg fibers* [4] are further discussed in Section 1.3. Thesis 1 takes benefit of such simulations in the design of leaking mode free photonic crystal fibers. The other equation derived from the Helmholtz equation, called the Nonlinear Schrödinger equation, determines the spectral and temporal evolution of pulses propagating along the fiber. The most important phenomena in the context of pulse propagation such as dispersion and nonlinearities are discussed in more detail. In Section 1.2 an introduction to the different *Types of photonic crystal fibers* is given [5, 6], which are extensively used tools for influencing dispersive and nonlinear effects in a wide range. Photonic crystal fibers are in the focus of Thesis 1 and 2. The Nonlinear Schrödinger equation provides the basis of the simulations for Thesis 2, and also for the *Simulation of pulse propagation in fiber lasers* [7], in Section 1.4. This latter section is aimed to help the understanding of the complex behavior of fiber lasers, corresponding to Thesis 3. The last section in this chapter is a short review of the theory of *Autocorrelation measurements* extensively used in our experimental work for the characterization of the temporal pulse duration [8].

1.1 Theory of pulse propagation in optical fibers

From Maxwell's equations one can obtain the wave equation that describes light propagation in optical fibers [1]:

$$\nabla \times \nabla \times \mathbf{E} = -\frac{1}{c^2}\frac{\partial^2 \mathbf{E}}{\partial t^2} - \mu_0 \frac{\partial^2 \mathbf{P}}{\partial t^2}, \tag{1.1}$$

where $\mathbf{E}$ is the electric field, c is the speed of light in vacuum, μ_0 is the vacuum permeability and $\mathbf{P}$ is the induced electric polarization.

The response of any dielectric to light becomes nonlinear for intense electromagnetic fields. On a fundamental level, the origin of nonlinear response is related to anharmonic motion of bound electrons under the influence of an applied field. As a result, the total polarization $\mathbf{P}$ induced by electric dipoles is not linear in the electric field, but satisfies the more general relation

$$\mathbf{P} = \varepsilon_0 \left(\chi^{(1)} \cdot \mathbf{E} + \chi^{(2)} : \mathbf{EE} + \chi^{(3)} \vdots \mathbf{EEE} + \dots \right), \tag{1.2}$$

where ε_0 is the vacuum permittivity and $\chi^{(j)}$ is the jth order susceptibility.

It is necessary to make several assumptions to solve the wave equation. First, the nonlinear part of $\mathbf{P}$ is treated as a perturbation to the linear part. Secondly, the fiber losses are regarded small, thus the dielectric constant, $\varepsilon(\omega) = 1 + \chi$, is also treated in a perturbative manner. $\nabla \times \nabla \times \mathbf{E}$ is approximated with $-\nabla^2 \mathbf{E}$, assuming $\nabla \mathbf{E} = 0$. It is also a simplification when the field is assumed to maintain its polarization along the fiber length, so that a scalar approach is valid, although this does not hold for birefringent media. Optical fibers are typically weakly birefringent, and the polarization effects are usually neglected. Furthermore, the slowly varying envelope approximation is adopted.

By separating the rapidly varying part of the electric field (Eq. 1.3) and using the Fourier transformation $\tilde{E}(\mathbf{r}, \omega) = \mathcal{F}(E(\mathbf{r}, t))$, the wave equation can be transformed to the so-called Helmholtz equation (Eq. 1.4).

$$\mathbf{E} = 1/2\hat{\mathbf{e}}[E(\mathbf{r}, t)\exp(-i\omega_0 t) + c.c.] \tag{1.3}$$

$$\nabla^2 \tilde{E} + \varepsilon(\omega)k_0^2 \tilde{E} = 0, \tag{1.4}$$

where $\hat{\mathbf{e}}$ is the polarization unit vector, $\mathbf{r}$ is the space coordinate, t is time, ω is the frequency, ω_0 is the central frequency, $c.c.$ denotes complex conjugate, $k_0 = \omega/c$, and from the dielectric constant the linear and nonlinear refractive indices can be deduced as $\varepsilon(\omega) = (n + \Delta n)^2$. The Helmholtz equation can be solved by the method

of separating the variables in the following form.

$$\tilde{E}(\mathbf{r}, \omega) = F(x, y)\tilde{A}(z, \omega) \exp(i\beta_0 z), \tag{1.5}$$

where $F(x, y)$ is the transverse modal distribution, $\tilde{A}(z, \omega)$ is a slowly varying function of z describing the spectral dependence and $\exp(i\beta_0 z)$ refers to longitudinal propagation. (β_0 is the wave number, z is the coordinate parallel to the fiber axis, x and y are the transverse coordinates.)

The Helmholtz equation leads to the following two equations for $F(x, y)$ and $\tilde{A}(z, \omega)$.

$$\frac{\partial^2 F}{\partial x^2} + \frac{\partial^2 F}{\partial y^2} + [\varepsilon(\omega)k_0^2 - \tilde{\beta}^2]F = 0, \tag{1.6}$$

$$2i\beta_0\frac{\partial\tilde{A}}{\partial z} + (\tilde{\beta}^2 - \beta_0^2)\tilde{A} = 0. \tag{1.7}$$

The eigenvalue $\tilde{\beta}$ of Eq. 1.6 includes the propagation constant, $\beta(\omega)$, and its perturbation, $\Delta\beta$. $\beta(\omega)$ can be expanded to a Taylor-series to describe the different orders of dispersion, see Eq. 1.10. The perturbation term depends on the modal distribution and the nonlinear refractive index, $\Delta\beta = \Delta\beta(\Delta n, F(x, y))$.

After all, by using $\tilde{\beta}$, the Fourier transformation of Eq. 1.7 leads to the propagation equation for $A(z, t)$, the so-called Nonlinear Schrödinger equation:

$$\frac{\partial A}{\partial z} + \beta_1\frac{\partial A}{\partial t} + \frac{i\beta_2}{2}\frac{\partial^2 A}{\partial t^2} = \frac{g - \alpha}{2}A + i(\gamma + \frac{i}{2}\alpha_2)|A|^2 A, \tag{1.8}$$

where

$$\gamma = \frac{n_2\omega_0}{cA_{\text{eff}}}. \tag{1.9}$$

The term including γ, the nonlinear parameter, is self-phase modulation with n_2 denoting the nonlinear refractive index, A_{eff} denoting the effective core area of the fiber and $|A|^2$ representing the optical power. g and α are the gain and loss, respectively, and α_2 is the parameter for two-photon absorption. The dispersion can be expressed through the $\beta(\omega)$ propagation constants, so generally the terms proportional to β_1 and β_2 can be completed with higher order terms of the expansion of $\beta(\omega)$ into it's Taylor-series. The Nonlinear Schrödinger equation can be extended by further nonlinear terms such as Raman scattering, self-steepening etc.

Dispersion

The Taylor-series of the $\beta(\omega)$ propagation constant is the following:

$$\beta(\omega) = \beta_0 + \beta_1(\omega - \omega_0) + \frac{1}{2}\beta_2(\omega - \omega_0)^2 + \frac{1}{6}\beta_3(\omega - \omega_0)^3 + \dots. \tag{1.10}$$

The dispersion parameters are defined according to this expansion, with the multiplication of the distance (L). The first term gives an initial phase factor, $\Phi_0 = \beta_0 L$, the second is responsible for the group delay, GD$= \beta_1 L$, $\beta_1 = 1/v_g$ where v_g is the group velocity, the next term is responsible for the group delay dispersion, GDD$= \beta_2 L$ or group velocity dispersion (GVD), and the last one is for the third order dispersion, TOD$= \beta_3 L$ etc. Another way to take chromatic dispersion into account is through the refractive indices $n(\omega)$, which can be given as Sellmeier-equations for different materials. As an example, see Fig. 1.1 (a) for the refractive index and the calculated $\beta_2 =$GDD$/L$ function in the near infrared region.

$$\beta(\omega) = n(\omega) \cdot \frac{\omega}{c}. \tag{1.11}$$

In some fields of optics dispersion is introduced as derivatives with respect to wavelength. The D parameter (usually given in [ps/nm/km] units) is defined as follows:

$$\text{D} = \frac{d\beta_1}{d\lambda} = -\frac{2\pi c \beta_2}{\lambda^2} \approx \frac{\lambda}{c}\frac{d^2 n}{d\lambda^2} \tag{1.12}$$

If D is less than zero (GVD> 0), the medium is said to have normal dispersion. If D is greater than zero (GVD< 0), the medium has anomalous dispersion. If a light pulse is propagated through a normally dispersive medium, the higher frequency components travel slower than the lower frequency components. The pulse is said to be *positively chirped*, i.e. increasing in frequency with time and vice versa. This causes a short pulse to spread in time, as it is plotted in Fig. 1.1 (b). It is to be mentioned, that for a Fourier transform limited pulse, i.e., a pulse with zero chirp, both positive and negative GVD have the same effect in case of a symmetrical spectrum. And another important feature is that the broadening caused by a fix amount of GDD on a shorter (Gaussian) pulse is more significant due to the relation $T = T_0\sqrt{1 + \text{GDD}^2/T_0^2}$, where T is the half-width of the chirped pulse, while T_0 is the half-width of the transform-limited pulse at $1/e$ intensity. The TOD leads to further modulation of the pulse shape, as plotted on the same graph. There are generally two sources of dispersion: material dispersion and waveguide dispersion. Material dispersion comes from a frequency-dependent response of a medium to electromagnetic waves. For example, material dispersion leads to undesired chromatic aberration in a lens or the separation of colors in a prism. Waveguide dispersion occurs when the speed of a wave in a waveguide (such as an optical fiber) depends on its frequency for geometric reasons, independent of any frequency dependence of the materials from which it is constructed. More generally, waveguide dispersion can occur for waves propagating through any inhomogeneous structure (e.g. a photonic
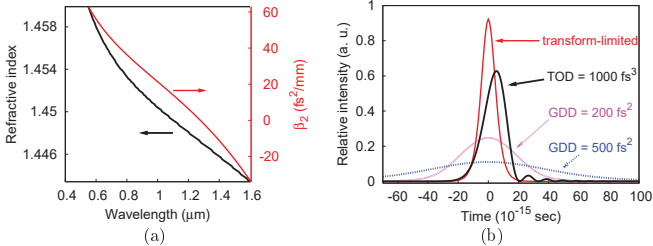
Figure 1.1: (a) Refractive index and dispersion (β_2) of fused silica, calculated from the Sellmeier equation, and (b) the effect of dispersion (GDD, TOD) on a $\sim$ 20 fs transform-limited pulse.

crystal), whether or not the waves are confined to some region. In general, both types of dispersion may be present, although they are not strictly additive [2].

Waveguide dispersion can be used to shift the zero-dispersion wavelength (1.3 µm, see Fig. 1.1 (a)) of silica fibers. This can be done by appropriately changing the cladding structure, especially by creating a photonic crystal structure in the cladding, and thus significantly modifying the dispersion curve.

A similar effect to chromatic dispersion due to a somewhat different phenomenon is *modal dispersion*, caused by a waveguide having multiple modes at a given frequency, each with a different speed. A special case of this is *polarization mode dispersion*, which comes from a superposition of two modes that travel at different speeds due to random imperfections that break the symmetry of the waveguide.

Nonlinearity

The nonlinear response of dielectric materials to the electric field is described by Eq. 1.2. The linear susceptibility $\chi^{(1)}$ represents the dominant contribution to $\mathbf{P}$, and its effects are characterized by the refractive index n and the attenuation coefficient α. The second order susceptibility $\chi^{(2)}$ is responsible for such nonlinear effects as second-harmonic and sum-frequency generation. However, for media with inversion symmetry at the molecular level, such as SiO_2, $\chi^{(2)}$ vanishes. As a result, silica fibers normally do not exhibit second-order nonlinear effects. The third order susceptibility $\chi^{(3)}$ is responsible for phenomena such as nonlinear refraction, third-harmonic generation, and four-wave mixing. To generate new frequencies by the latter two effects the phase-matching condition has to be fulfilled. The most

common nonlinear effect in optical fibers is thus the nonlinear refraction, i.e., the intensity dependence of the refractive index. The refractive index is given as:

$$n(\omega, |E|^2) = n(\omega) + n_2 I, \tag{1.13}$$

where $I = \frac{\varepsilon_0 cn}{2}|E|^2$ is the optical intensity, and n_2 is the nonlinear refractive index, related to the real part of the fourth-rank tensor $\chi^{(3)}$ as $n_2 = 3/(8n)\Re(\chi^{(3)}_{xxxx})$. n_2 is typically $2.2 - 3.4 \times 10^{-20}$ m^2/W in silica fibers. It is to be noted, that the tensorial nature of $\chi^{(3)}$ influences the polarization properties of the beams through nonlinear birefringence. The intensity dependence of the refractive index leads to phenomena such as self-phase modulation (SPM) and cross-phase modulation (XPM). SPM refers to self-induced phase shift experienced by the optical field during propagation in the nonlinear material, by

$$\Phi_{\mathrm{NL}}(t) = n_2 I(t) k_0 L. \tag{1.14}$$

This phase shift leads to spectral broadening of ultrashort pulses, as shown in Fig. 1.2. It is to be mentioned that nonlinear and dispersive effects might can-
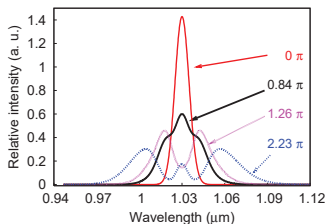
Figure 1.2: Effect of self-phase modulation proportional to the nonlinear phase shift.

cel out in a medium, this phenomenon results in the so-called solitons. These are self-reinforcing waves that maintain their shape during propagation.

Although Eq. 1.7 is successful in explaining pulse propagation in most cases, it has to be modified to include other nonlinear effects such as the inelastic scattering processes of stimulated Raman and Brillouin scattering. These effects might have an important role in highly nonlinear fibers for example in continuum generation.

For further reading on nonlinear phenomena in optical fibers, see [1].

1.2 Types of photonic crystal fibers

Conventional optical fibers consist of a core surrounded by a cladding layer, typically both made of glass, with the cross-section uniform along the fiber length. To confine light in the core, the refractive index of the core (e.g. by doping with GeO_2) must be greater than that of the cladding. The waveguiding mechanism works until the angle of incidence is smaller than the critical angle for total internal reflection. The boundary between the core and cladding may either be abrupt, as in step-index fibers, or gradual, as in graded-index fibers. Fibers which can only support a single transversal mode are called *single-mode fibers* (SMF). Multi-mode fibers generally have a larger core diameter, and are used for applications where high power should be transmitted.

Photonic crystals are composed of periodic (dielectric) structures, of high and low refractive indices, with a periodicity close to the visible wavelength region (0.1-10 µm). In general, *photonic crystal fibers* (PCFs) or *micro-structured fibers* have a two-dimensional (2D) photonic crystal structure in the cladding. Considering the principle of propagation in the fiber there are two types of optical fibers.

In the first type, also known as *index-guiding fibers*, the light confinement in the core is based on total internal reflection, as in conventional optical fibers, see Fig. 1.3 (a). The difference of the core and cladding refractive indices, that determines single-mode behavior[1], can be changed by adding an array of microscopic air-channels into the cladding running along the fiber length. If the air holes in the cladding are tiny enough, the effective refractive index of the cladding differs from the core index very slightly, which gives a small V-parameter even at reasonably high core diameters (see middle picture in Fig. 1.3 (a) for the structure, and Fig. 1.4 (a) for the refractive index profiles). Such *large mode area* (LMA) *fibers* support a single mode while being able to transmit high power with reduced nonlinearity (note for the core area dependence of γ, Eq. 1.9). On the other hand, if the air/silica fraction is high in the cladding, the index difference, and thus the numerical aperture gets high. The numerical aperture determines the critical angle of incidence for coupling light into the core of the fiber. In order to achieve high nonlinearity in the fiber, the core size is reduced. For a fixed collimated beam diameter the focused spot size has to be reduced, but this can only be done as a trade-off with the focus length of the lens,

---

[1]The so-called V-parameter determines the number of modes supported by the fiber. $V = k_0 r_{core} \sqrt{n_{core}^2 - n_{clad}^2}$, where $k_0 = 2\pi/\lambda$, λ is the wavelength, r_{core} is the core radius, n_{core} is the core and n_{clad} is the cladding refractive index, respectively. For a step-index fiber, the single-mode condition is $V < 2.405$ [1].

i.e., increased numerical aperture. As a consequence, highly *nonlinear* (NL) *fibers* are made of extremely small core sizes (of $\sim 1-2$ µm diameter) and high air/silica fraction for the cladding, to enable high coupling efficiency. The scheme of the cross-section of such a fiber, and the refractive index profile can be seen in the bottom picture in Fig. 1.3 (a), and in Fig. 1.4 (a), respectively. A photo of supercontinuum, generated in a highly nonlinear PCF by a Ti:sapphire laser (@800 nm) is shown in Fig. 1.5. The energy of the ~ 100 fs pulses was relatively low, a few nano-Joules, and with this commercially available fiber it was possible to generate a broad spectrum light in the visible. The hexagonal symmetry of the fiber can be observed on the far field modal distribution.

The other type of photonic crystal fibers considering the principle of propagation are *photonic-bandgap fibers* (PBFs). The confinement of light in the core is based on the photonic bandgap (PBG) structure of the cladding, prohibiting propagation for a given incident angle and wavelength range. This is similar to dielectric multilayer structures, where layers have $\sim \lambda/4$ thickness and reflect $\sim 100\%$ of the light by constructive interference, according to the Bragg condition. A special type of PBFs is the Bragg PBF in which the cladding is formed by concentric rings of dielectric layers. The waveguiding mechanism in PBFs is illustrated in Fig. 1.3 (b). In these fibers the refractive index of the core can have any value, light can even be guided in a hollow-core (HC). The refractive index profile of such a fiber is shown in Fig. 1.4 (b). The effective refractive index [2] (n_{eff}) for the fundamental mode is below the core index, in case of HC fibers it is typically ~ 0.98, and it is dependent on the angle of incidence and the wavelength. As a consequence, by changing the fiber structure the dispersion profile can be modified, even up to the third order [J1].

Over the past decade PCFs have attracted increasing interest in many fields as they offer greatly enhanced design freedom compared to standard optical fibers: they allow precise control of the nonlinear coefficient and the dispersion profile over a broad wavelength range. This gives rise to numerous applications, such as dispersion control and distortion-free delivery of ultrashort pulses by the elimination of nonlinear distortion in LMA PCFs or HC PBFs. Furthermore, they also permit studies of nonlinear pulse propagation in previously inaccessible parameter regimes.
Generally, PCFs are constructed by a similar method to other optical fibers: first, a set of precision manufactured glass capillaries and rods are stacked into a macroscopic "preform" of the desired micro-structure. This preform stack is then fused together and reduced in size by several orders of magnitude in a fiber-drawing tower.

---

[2] n_{eff} is related to the propagation constant (Eq. 1.10) as $\beta = k_0 n_{\text{eff}}$.
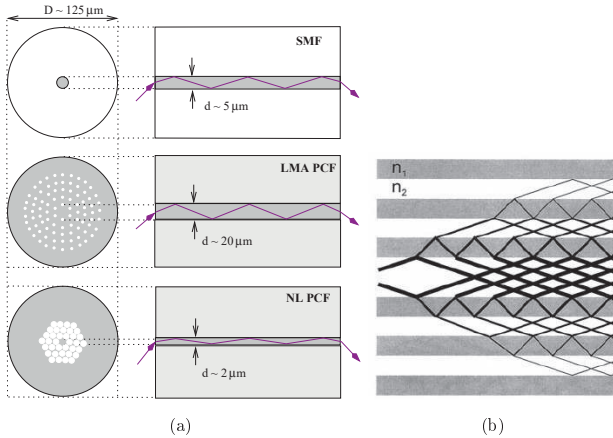
Figure 1.3: Structure of different types of optical fibers according to the principle of propagation. Confinement in the core might be based on total internal reflection (a), and on the photonic bandgap structure of the cladding [9] (b).

Figure 1.4: Index profile of fibers where the propagation is based on total internal reflection (a), and on the photonic bandgap structure of the cladding (b).

In this way, hundreds of kilometers of fiber can be produced from a single preform of ~ 1 m.

Figure 1.5: Photo of a supercontinuum generated in the visible wavelength region by our Ti:sapphire laser.

1.3 Simulation of fiber modes

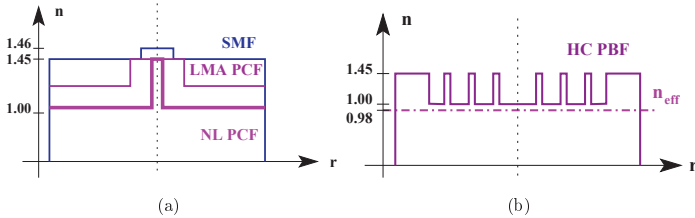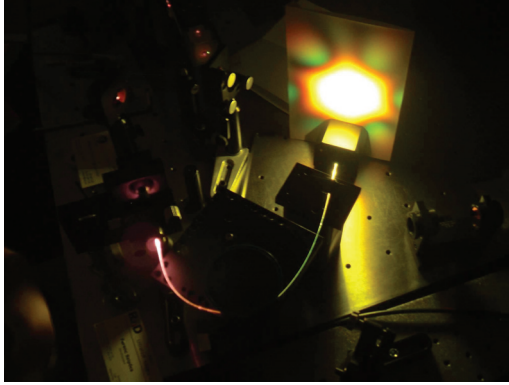Although some important properties of the guided modes in optical fibers can be qualitatively understood with the use of analytical approaches, the quantitative analysis of PCFs generally requires rigorous numerical methods [3]. Several powerful fully vectorial techniques have been recently adapted to simulations of light propagation in various classes of PCFs, including the plane wave expansion, the finite element method (FEM), the expansion in localized functions, the multipole technique, the source model technique, the finite difference time-domain method etc. One of the most widely used and successful approach is the FEM, which is able to provide information on important parameters such as mode field intensity profiles, the dispersion parameters, and various types of losses in good agreement with measurement data.

A simplified tool for calculating fiber modes and the bandgap in Bragg fibers is the transfer matrix method (TMM). This method is valid for fibers with cylindrical symmetry. Comparison of TMM and FEM calculations were carried out as part of an effort to find efficient and reliable simulations for fiber modes.

1.3.1 The finite element method

The finite element method is a numerical technique for finding approximate solutions of partial differential equations and integral equations.

To determine the transversal fiber modes of a PCF, the propagation constants and the electric field distributions of the guided modes are calculated from the following generalized eigenvalue equations:

$$
\left[\begin{array}{cc} \nabla_\perp \times \nabla_\perp \times -k_0^2 n^2(\vec{r}) & 0 \\ 0 & 0 \end{array}\right] \left[\begin{array}{c} \vec{E}_\perp \\ E_z \end{array}\right] = -\beta^2 \left[\begin{array}{cc} 1 & \nabla_\perp \\ \nabla_\perp & \Delta + k_0^2 n^2(\vec{r}) \end{array}\right] \left[\begin{array}{c} \vec{E}_\perp \\ E_z \end{array}\right],
\tag{1.15}
$$

where the eigenvector $\vec{E} = [\vec{E}_\perp, E_z]$ is the instantaneous electric field vector in the PCF cross-section. The eigenvalue is the mode propagation constant, β, and k_0 is the wave number. It is assumed that the z and time dependence of all fields is $\exp[i(\omega t - \beta z)]$.

The basic idea is to replace the infinite dimensional linear problem with a finite dimensional version. For this purpose one chooses a grid or mesh to discretize the boundary value problem in a finite dimensional space, called elements, for the appropriate geometric boundary conditions. The grid consists of triangles or curvilinear elements. After that, basis functions are chosen. After this step, we have concrete formulae for a large but finite dimensional linear problem whose solution will approximately solve the original boundary value problem. As the underlying grid becomes finer and finer, the solution of the discrete problem will converge to the solution of the original boundary value problem.

In order to find the eigenpairs of the above equation, an eigensolver such as the Arnoldi method and for solving the linear system of equations a solver such as the asymmetric multifrontal method can be used. Using the spline representation of the fiber cross section as input data, a mesh for finite element calculations is generated as seen in Fig. 1.6.

A typical mesh in [3] is composed of ~ 600000 triangular elements (depending on the structure) and the convergence test on the fundamental mode shows that the calculated value of the effective index is stable on the sixth decimal place.
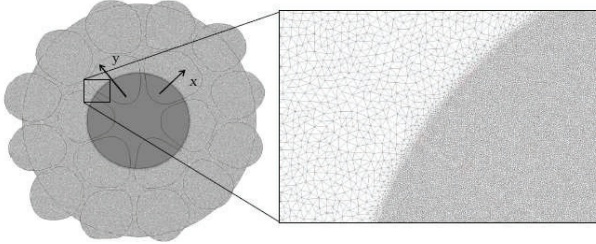
Figure 1.6: 2D mesh on a HC PBF for the FEM simulation (mesh is denser around the object of interest) [3].

1.3.2 The transfer matrix method of Bragg fibers

During our investigations of fiber modes in PBFs, we made an effort to find simpler and less time-consuming simulation methods compared to FEM. For fibers with cylindrical symmetry, i.e. consisting of concentric rings of dielectric layers, an effective simulation method is discussed in [4], called transfer matrix method (TMM). This method is able to calculate the transversal field distributions for a fixed β value. As a verification of reliability the results on the incident angle in a PBF with cylindrical symmetry were compared by the two methods.

By considering cylindrical coordinates, the field components E_r and H_Θ can be expressed with E_z, and H_r and E_Θ can be expressed with H_z. The solution of the Helmholtz equation (Eq. 1.4) in homogeneous media for these components are:

$$E_z = [AJ_l(kr) + BY_l(kr)]\cos(l\Theta + \phi) \tag{1.16}$$

$$H_z = [CJ_l(kr) + DY_l(kr)]\cos(l\Theta + \psi), \tag{1.17}$$

where $k = \sqrt{\omega^2\mu\varepsilon - \beta^2}$, and for the fundamental mode $l = 0$. At the boundaries the field components E_z, E_Θ, H_z and H_Θ have to be continuous. The boundary conditions lead to a matrix equation for the A, B, C, D parameters. Considering TM mode, i.e., $H_z = 0$ in the core, $A = 1$ and $B = C = D = 0$, as $Y_0(r = 0) = -\infty$. The A, B, C, D coefficients in the first cladding layer are calculated by the following matrix product:

$$\begin{pmatrix} A_1 \\ B_1 \\ C_1 \\ D_1 \end{pmatrix} = M^{-1}(k_2 r_c)M(k_1 r_c) \begin{pmatrix} 1 \\ 0 \\ 0 \\ 0 \end{pmatrix} \tag{1.18}$$
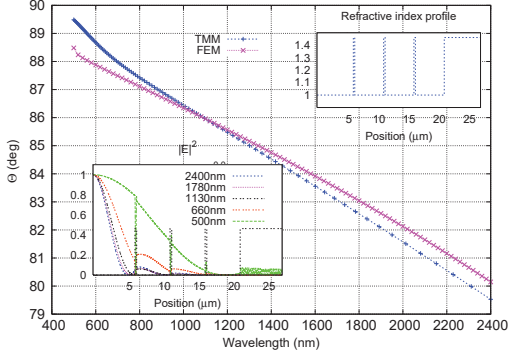
18

Figure 1.7: Comparison of the TMM and FEM calculation results on a HC PBF.

The M matrices contain terms with $J_o(k_i r)$, $Y_o(k_i r)$, and their derivatives $J'_o(k_i r)$, $Y'_o(k_i r)$, with $i = 1, 2$ and $r = r_c$ the boundary of the core. Similar matrix equations hold for all of the cladding layers so the A_i, B_i, C_i, D_i coefficients are determined by the $M(k_i r_i)$ and $M(k_{i+1} r_i)$ matrices, where i indexes the layer boundaries.

The drawback of this method is that to calculate the field distribution, it is necessary to know k_1 (or equivalently the Θ_0 angle of incidence)[3]. So the modes that are realistically confined in the core can only be determined by the minimization of the field intensity in the outer layer, that corresponds to energy loss of the propagating mode.

In Fig. 1.7 calculation results were shown on the hollow-core Bragg photonic bandgap fiber structure, which was used for the simulation in Chapter 2, in accordance with Fig. 2.7. In the upper inset one can find the refractive index profile of the Bragg fiber. The lower inset shows mode field intensity distributions calculated at different wavelengths after the optimization of the angle of incidence for maximal confinement in the core. It can be seen, that at 500 nm, the field is not zero in the outer layer, thus the fiber is lossy. The main plot shows the obtained angle of incidence as a function of wavelength, compared to results calculated by the FEM. The loss of the fiber could be calculated from the ratio of the field leaking to the outer layer to the part, that is confined by the cladding. However, as we found the optimization complicated and the agreement with the results with FEM not satisfying, we carried on with the simulations on fiber modes by the FEM.

---

[3]The propagation constant for the structure is $\beta = n_c k_1 \sin\Theta_0 = n_i k_i \sin\Theta_{i-1}$ for each layer.

1.4 Simulation of pulse propagation in fiber lasers

Passively mode-locked fiber lasers represent a dissipative nonlinear system. Their theoretical modeling is based on the Ginzburg-Landau equation (GLE) or extensions like the Swift-Hohenberg equation, where the actions within the cavity are averaged based in the assumption of small changes during one round-trip [10]. The solutions are the stable attractors that depend on the system parameters (e.g. net-cavity dispersion) rather than initial conditions. Beside the analytical research based on the GLE, a numerical approach of following the pulse inside a cavity by transmitting it through each element has been developed [7]. The numerical modeling of fiber lasers based on a non-distributed model makes fewer assumptions, it allows large pulse changes during one round-trip, and maintains the possibility of studying the intra-cavity pulse evolution.

Fiber lasers consist of a gain fiber, a saturable absorber element (e.g. a saturable absorber mirror) that is necessary for initiating pulse formation and mode-locking, an output coupler introducing some loss, dispersion compensation (e.g. a grating pair) and single-mode fiber pieces. These optical components affect the spectral and temporal profile of the envelope function that propagates through them. For simulating the pulse formation, an initial envelope function is evolved through the different optical elements subsequently, in many round-trips, until the pulse shape converges to a stable solution. The initial envelope function might be a Gaussian or other type of pulse or a random field distribution, both generated by giving a certain spectrum and adding an appropriate spectral phase.

The optical components are taken into account in the following way.

Single mode fibers and the gain fiber are described by the Nonlinear Schrödinger equation (Eq. 1.8) and are numerically solved by the so-called Split-step Fourier method [1].

The gain (g), used in the Nonlinear Schrödinger equation follows a phenomenological description for the saturation of the population inversion:

$$g = \frac{g_0}{1 + \mathbb{E}/\mathbb{E}_{\mathrm{sat}}}. \tag{1.19}$$

g_0 is the small signal gain (typically ~ 30 dB/m), $\mathbb{E}$ and $\mathbb{E}_{\mathrm{sat}}$ are the pulse energy and the saturation energy, respectively. In the generation of ultrashort pulses the bandwidth of the gain should be included. In Yb fibers it is usually described by a parabolic frequency dependence around 1.03 µm, with 40 nm FWHM. Spectral filtering by other elements may also be included in the model, similarly.

The dispersion compensation is implemented as a phase shift in Fourier space.

According to the dispersion term in Eq. 1.8, Section 1.1, it can be written as $A(z, \omega) = A(0, \omega) \cdot \exp(i\beta(\omega)z)$. The dispersion coefficients are included in $\beta(\omega)$ (see Eg. 1.10).

The saturable absorber (mirror) is modelled by a transmittance, T (/reflectance, R) given by the following equations.

$$T = 1 - R; \quad R = R_{\text{unsat}} + R_{\text{sat}} \cdot \left(1 - \frac{1}{1 + \mathbb{P}_{\text{inst}}/\mathbb{P}_{\text{sat}}}\right). \tag{1.20}$$

The realistic finite response time of the absorber is neglected as it is assumed to be much lower than the pulse duration. For low power signals, when the saturable absorber is unsaturated, it introduces loss i.e., the unsaturated loss, R_{unsat}. For pulses, emerging from quantum noise, the loss is reduced, proportionally to $\mathbb{P}_{\text{inst}}/\mathbb{P}_{\text{sat}}$. $\mathbb{P}_{\text{inst}}$ and $\mathbb{P}_{\text{sat}}$ are the instantaneous power of the pulse, and the saturation power, respectively, with $\mathbb{P}_{\text{inst}} = |A|^2$. After several round-trips in the resonator with gain, the pulse saturates the absorber. The transmission curve is maximal at the peak of the pulse and introduces higher loss at the edges, resulting in pulse shaping known as *self-amplitude modulation*.

Varying the simulation parameters leads to different pulse formation mechanisms. Investigations in [7] show that by changing $\mathbb{E}_{\text{sat}}$ and the net-cavity dispersion (GDD$_{\text{net}}$) may result in different mode-locking regimes (see Section 4.2 for an explanation on mode-locking regimes). For a lower value of $\mathbb{E}_{\text{sat}}$ and GDD$_{\text{net}}$ the pulses show the characteristics of the stretched-pulse regime. For higher values of both parameters the resulting pulse has parabolic shape and parabolic spectral phase (linear chirp, constant GVD) implying self-similar mode-locking.

The intra-cavity pulse evolution in the above regimes are shown in Fig. 1.8. The horizontal axis represents small spatial segments of the cavity in which the temporal shape of the pulse is characterized. The temporal intensity distributions are plotted along the vertical axis encoded by colors (red shows high, blue shows low intensity). For $\mathbb{E}_{\text{sat}} = 100$ pJ, GDD$_{\text{net}} = -0.002$ ps^2 the pulse width has two minimum points during the roundtrip in the resonator, which is typical for stretched-pulse mode-locking. In contrast, $\mathbb{E}_{\text{sat}} = 400$ pJ and GDD$_{\text{net}} = 0.0045$ ps^2 results in only one minimum point, which is the case in similariton lasers.

1.5 Autocorrelation measurement

The most common technique for characterizing ultrashort laser pulses is the measurement of the autocorrelation (AC) function. The autocorrelation measurement is usually based on a nonlinear process such as second-harmonic generation. In
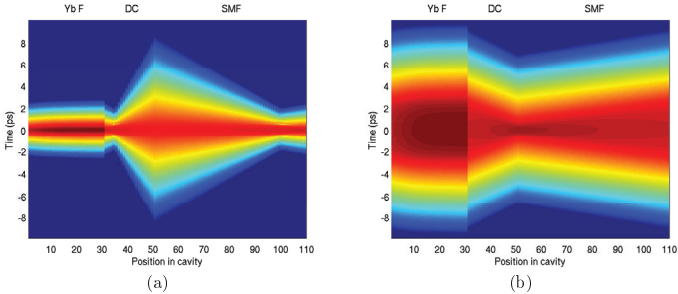
Figure 1.8: Intra-cavity pulse evolution for (a) $\mathbb{E}_{\mathrm{sat}} = 100$ pJ, $\mathrm{GDD}_{\mathrm{net}} = -0.002$ ps^2, typical for a stretched pulse laser (b) $\mathbb{E}_{\mathrm{sat}} = 400$ pJ and $\mathrm{GDD}_{\mathrm{net}} = 0.0045$ ps^2, typical for a similariton laser. Yb F, DC, and SMF denote Yb fiber, dispersion compensation and single mode fibers, respectively, i.e. the components in the cavity. The saturable absorber and the resonator losses are placed between the Yb F and DC, which can be identified as an intensity reduction in the graph. (The results are in accordance with [7].)

this case it is referred to as a second-order autocorrelation measurement [8]. In this method the pulse is divided by a beam splitter and the two beams are sent through a nonlinear crystal with variable delay (τ) between the two beams. A second-harmonic signal is generated in the crystal when the two pulses overlap. Measuring the second-harmonic power as a function of time delay produces the AC trace. The width of this trace is related to the pulse duration, however, the exact relationship depends on the pulse shape.

The second-order interferometric autocorrelation function, recorded by a slow detector is:

$$I_{\mathrm{AC}}(\tau) = \int_{-\infty}^{\infty} |(E(t) + E(t-\tau))^2|^2 dt. \tag{1.21}$$

In the case of the phase being averaged over time, the signal recorded by a slow detector is the second-order intensity autocorrelation function:

$$I_{\mathrm{AC}}(\tau) = \int_{-\infty}^{\infty} I(t) \cdot I(t-\tau) dt. \tag{1.22}$$

The peak to background ratio in the interferometric and the intensity autocorrelations are 8:1 and 3:1, respectively.

2 Design of leaking mode free hollow-core photonic bandgap fibers

In this thesis a method for the proper design of photonic bandgap dielectric structures used at grazing incidence is proposed [T1]. The theory is based on the one-dimensional (1D) multilayer design (see Section 2.1). Different designs of one-dimensional photonic bandgap dielectric structures are compared, and as a result, dielectric laser mirrors are suggested to be used at grazing incidence (see Section 2.2). The model is extended to two-dimensional (2D) photonic bandgap dielectric structures and applied to all-silica hollow-core Bragg photonic bandgap fibers (HC Bragg PBFs). The principles of the elimination of leaking modes in realistic HC Bragg PBFs are described in Section 2.3. The results are compared to simulations done by the finite element method, that takes the realistic 2D cross-sectional structure into account. The qualitative agreement implies, that the 1D model is capable of giving estimates for the ideal design of such fibers. The conclusion is drawn is Section 2.4.

2.1 Theory of one-dimensional multilayer design

The behavior of photonic bandgap structures can be understood by regarding the partial waves reflected from the surfaces of the structure that add up to interfere [11]. For this, two kinds of phase shifts are considered. One of them directly comes from the wavelength (λ) dependence of the refractive index (n) and can be calculated as $\Phi(\lambda) = n(\lambda) \cdot L \cdot 2\pi/\lambda$, where L is the physical path length in the homogeneous media. The other kind of phase shift is on reflection and transmission on the surface of two media with different refractive indices. These are obtained by the Fresnel-formulae for reflection (r) and transmission (t) coefficients (see Equations (2.1-2.4)) where $\Theta_{in}, \Theta_r, \Theta_t$ are the incident, reflection and transmission angles, respectively, and P and S stand for the two polarizations. The phase shifts can be calculated as the arc-tangent of the ratio of the imaginary and the real parts of the square root of the Fresnel-coefficients ($\Phi_r = \arctan(\frac{\Im(\sqrt{r})}{\Re(\sqrt{r})})$) and the same holds for t).

$$r_P = \frac{n_1 \cos(\Theta_t) - n_2 \cos(\Theta_{in})}{n_1 \cos(\Theta_t) + n_2 \cos(\Theta_{in})} \tag{2.1}$$

$$r_S = \frac{n_1 \cos(\Theta_{in}) - n_2 \cos(\Theta_t)}{n_1 \cos(\Theta_{in}) + n_2 \cos(\Theta_t)} \tag{2.2}$$

$$t_P = \frac{2 \sin(\Theta_t) \cos(\Theta_{in})}{\sin(\Theta_{in} + \Theta_t) \cos(\Theta_{in} - \Theta_t)} \tag{2.3}$$

$$t_S = \frac{2 \sin(\Theta_t) \cos(\Theta_{in})}{\sin(\Theta_{in} + \Theta_t)} \tag{2.4}$$

Considering the interface between air ($n_1 = 1.0$) and silica ($n_2 \approx 1.45$), the reflection and transmission coefficients and phase changes are plotted as a function of the incident angle in Figure 2.1.

One can see that when light is incident at small angles all the phase changes on reflection as well as transmission are either $\Phi_{r,t} = 0$ or π. The only distinct region is when light propagates from the higher index region (n_2) to the lower index one (n_1) and Θ_{in} is high. One may assume that this is the case in PBGFs, where the incident angle is typically above $\sim 86°$. In contrary, according to Snell's law [4] the refracted angle (of a medium with higher refractive index than that of the incidence medium) never reaches the critical angle for total internal reflection (TIR) above which the phases would rapidly change.

In order to investigate different types of multilayer structures the relative phase shifts of the partial waves reflected from different penetration depths were calculated

---

[4]$n_0 \sin(\Theta_{in}) = n_1 \sin(\Theta_1) = n_2 \sin(\Theta_2)$, where Θ_{in}, Θ_1 and Θ_2 are the angles of refraction in the $n_0 = 1.0, n_1 = 1.45$ and $n_2 \geq 1.0$ layers, respectively. The critical angle for TIR could only be exceeded in a structure where $n_1 > n_0 > n_2$.
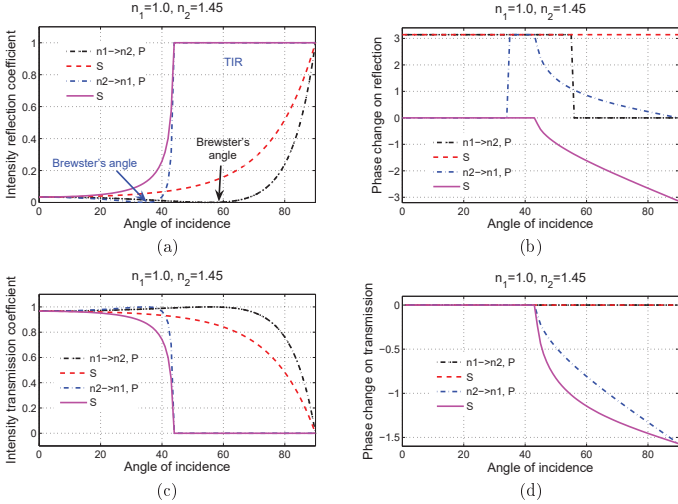
Figure 2.1: (a) Reflection and (c) transmission coefficients, (b) phase change on reflection and (d) phase change on transmission at an interface. Black and red lines refer to an interface where propagation is from the n_1 to the n_2 medium and blue and magenta lines refer to the opposite direction. Furthermore, black and blue lines refer to P polarization while red and magenta refer to S polarization.

along the reflected wavefront. These calculations were carried out on the structures that mimic the 2D HC Bragg photonic bandgap fibers, see Section 2.3, Fig. 2.8. The results give an insight of the origin of the different reflection bands for the slightly differing multilayer structures.

A short review is given in the following section of a more complicated and extensively used description of the behavior of multilayer structures, that is used for e.g. the calculation of the reflection band and dispersion profile of dielectric mirrors. The results of 1D simulations in Section 2.2 and 2.3 are calculated with this method.

2.1.1 Simulation of dielectric multilayer structures

The simulation of dielectric multilayer structures is based on the theory of thin film interference filters, to be read in [11].

First, a thin, plane parallel film covering a substrate is investigated, as shown in Fig. 2.2. In this arrangement a number of beams will be produced by the successive
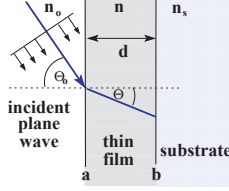
Figure 2.2: Plane wave entering a thin film

reflections on the surfaces. Considering plane waves the boundary conditions lead to the following relationship for the tangential components E, H of the electric ($\mathbf{E}$) and magnetic ($\mathbf{H}$) waves. Starting from boundary "b" the waves at boundary "a" can be expressed from the summation of waves propagating towards and backwards from the substrate and by adding the appropriate phase factors.

$$
\begin{pmatrix} E_a \\ H_a \end{pmatrix} = \begin{bmatrix} \cos\delta & i \cdot \sin\delta/\eta \\ i \cdot \sin\delta \cdot \eta & \cos\delta \end{bmatrix} \begin{pmatrix} E_b \\ H_b \end{pmatrix}
\tag{2.5}
$$

The phase factor accounting for the propagation in the thin film is:

$$
\delta = \frac{2\pi}{\lambda} dN \cos\Theta,
\tag{2.6}
$$

and the following further quantities are used. η, the optical admittance is introduced to describe the relationship between $\mathbf{E}$ and $\mathbf{H}$. For P waves the field vectors' components parallel to the boundary are H_y and E_x and for the S waves they are E_y and H_x. From the Maxwell-equations containing the curl of $\mathbf{E}$ and $\mathbf{H}$ the following is deduced:

$$
\eta_p = \frac{H_y}{E_x} = \frac{N}{c\mu\cos(\Theta)} = N \cdot \mathcal{Y} / \cos\Theta
\tag{2.7}
$$

$$
\eta_s = \frac{H_x}{E_y} = N \cdot \mathcal{Y} \cdot \cos\Theta
\tag{2.8}
$$

$$
\mathcal{Y} = (\varepsilon_0/\mu_0)^{1/2} = 2.6544 \cdot 10^{-3} \mathrm{S},
\tag{2.9}
$$

where $N = n - ik$ is the complex refractive index, c is the speed of light in vacuum, μ is the permeability, Θ is the refraction angle in the medium (here in the thin film). $\mathcal{Y}$ is the optical admittance of free space involving μ_0 and the permittivity, ε_0, in free space and we take the assumption that the relative permeability is unity at optical frequencies ($\mu_r = \mu/\mu_0 \approx 1$).

For the later calculations on thin films it is useful to introduce $Y = H_a/E_a$, the ratio of the electric and magnetic field components at surface of the (multi)layer structure, and $\eta_2 = H_b/E_b$ as the modified admittance of the substrate and η_1 denote the modified admittance of the thin film layer thus write Eq. (2.5) in the form

$$E_a \begin{bmatrix} 1 \\ Y \end{bmatrix} = \begin{bmatrix} \cos\delta & i \cdot \sin\delta/\eta_1 \\ i \cdot \sin\delta \cdot \eta_1 & \cos\delta \end{bmatrix} \begin{bmatrix} 1 \\ \eta_2 \end{bmatrix} E_b \qquad (2.10)$$

An assembly of layers can then be described by the product of successive matrices, in an order starting from the substrate towards the incident medium.

$$\begin{bmatrix} B \\ C \end{bmatrix} = \prod_{r=1}^{q} \begin{bmatrix} \cos\delta_r & i \cdot \sin\delta_r/\eta_r \\ i \cdot \sin\delta_r \cdot \eta_r & \cos\delta_r \end{bmatrix} \begin{bmatrix} 1 \\ \eta_m \end{bmatrix} \qquad (2.11)$$

where $r = 1 \ldots q$ is the index of the layers, and m refers to the substrate layer. The matrix product $\begin{bmatrix} B \\ C \end{bmatrix}$ is the characteristic matrix of the assembly and $Y = B/C$. Θ_r are determined by Snell's law ($N_0 \sin\Theta_0) = N_r \sin\Theta_r(\lambda)$) and δ_r are according to Eq. (2.6) using the parameters of the appropriate layers.

The physical quantities that are calculated are e.g. the reflection, transmission, (absorption), phase delay and by derivations the group delay dispersion [5] as a function of wavelength (λ) and possibly angle of incidence etc.

---

[5] see Section 1.1 for the definition of GDD

2.2 Analysis of one-dimensional structures

2.2.1 Motivation

Multilayer (ML) structures designed on the basis of the Bragg condition are extensively used as high reflectors for neutrons and electromagnetic waves. While such mirrors are usually designed for normal incidence for most of the electromagnetic spectrum, for neutrons and X-rays they are designed to be used at grazing incidence for the following reason. The refractive index difference between the alternating layers in these wavelength regions is relatively low and it can be shown that high reflectance in a meaningful bandwidth can only be obtained at a high value of angle of incidence [11]. Typically multilayers are composed of Ni/Ti and Mo/Si and they are used at $85 - 90°$ angle of incidence ($1 - 5°$ and $< 1°$ according to their conventional notations) for neutrons and X-rays, respectively.

A technique to further increase the bandwidth of grazing incidence neutron and X-ray mirrors is "chirping" i.e. properly varying the Bragg period of the multilayer structure [12]. This method has also been successfully applied in the design of ultrabroadband dielectric mirrors, – used at normal incidence – for broadly tunable and ultrashort pulse femtosecond systems [13, 14].

Interestingly, grazing incidence quarter-wave dielectric mirrors have not been applied in the construction of laser resonators yet, despite the fact that the bandwidth of such mirrors is considerably higher than for normal incidence ones (this refers to S-polarized light only). The use of grazing incidence dielectric mirrors instead of ultrabroadband chirped mirrors could be desirable in some applications because of the following reasons: (i) grazing incidence dielectric mirrors require much lower number of layers than chirped mirrors to reach the same reflectivity (this might be advantageous in the near IR regime where the physical thickness of the layers is relatively high) and (ii) periodic grazing incidence structures have a smooth group delay dispersion (GDD) function, free from oscillations and (iii) periodic grazing incidence mirrors exhibit much lower group delay upon reflection, consequently they exhibit considerably lower absorption and scattering loss as well [15]. As a matter of fact, the bandwidth of periodic grazing incidence dielectric mirrors is comparable to that of normal incidence chirped mirrors built of the same dielectric layer materials. However, besides the constrains on the cavity geometry a disadvantage of the former could be that they do not provide considerable negative GDD upon reflection that is preferred in mirror dispersion controlled laser systems [16].

2.2.2 Design of grazing incidence dielectric mirrors

Periodic dielectric structures exhibit a photonic bandgap when the beams partially reflected on the layer interfaces meet in phase upon reflection (Bragg condition). In case of two valued periodic index profiles, the highest reflectivity and the highest bandwidth is obtained when the alternating high (H) and low (L) index dielectric layers have quarter-wave optical thicknesses [11, 15]. However, the full bandwidth offered by broadband solid state gain media such as Ti:sapphire could not be utilized until properly designed aperiodic dielectric mirrors known as chirped mirrors were devised [13, 14, 16]. They provide a higher bandwidth compared to quarter-wave dielectric mirrors, a smooth, engineerable dispersion profile with anomalous dispersion over most of the bandwidth, which allowed construction of mirror dispersion controlled femtosecond pulse solid state laser oscillators delivering sub-10-fs pulses directly at the laser output [16]. In all of these applications, the dielectric mirrors were used at nearly normal incidence of light. In the followings we show that similarly high bandwidth and a smooth dispersion profile can be obtained when periodic dielectric mirrors are used for grazing incidence of light.

Generally, at oblique incidence, there are two facts that have to be considered at the design stage: first, the optical thickness of the layers have to be corrected by the cosine of the angle of refraction in the given layer, which practically introduces a blue shift of the reflection band, secondly, the refractive index difference between the layers and the polarization of the electromagnetic wave (S- or P-polarization) determine the useful bandwidth of quarter-wave high reflectors.

In order to compare the optical performance of different multilayer designs, we have calculated the reflectivity, the group delay, and the GDD as a function of wavelength of the following structures. A periodic multilayer structure of 24 periods of layer pairs (with $n_H = 2.315$ and $n_L = 1.45$ refractive indices) was designed for normal incidence light obeying the quarter-wave condition, for $\lambda_0 = 790$ nm central wavelength (see Fig. 2.3 (a)), resulting in a ~ 230 nm wide bandgap. A similar structure was chirped and optimized in Ref. [13] in order to broaden the bandgap and smooth the dispersion function of the chirped structure. This resulted in an extended reflection band ranging from 660 to 1060 nm (R> 99%) and a monotonous group delay vs wavelength function with some oscillations in the GDD (see Fig. 2.3 (b)). Another periodic ML structure with similar parameters is designed for grazing incidence (80°) S-polarized light. In this case the bandgap extends over the 660 to 1000 nm wavelength range with a smooth dispersion profile changing sign in the middle of the bandgap (see Fig. 2.3 (c)).
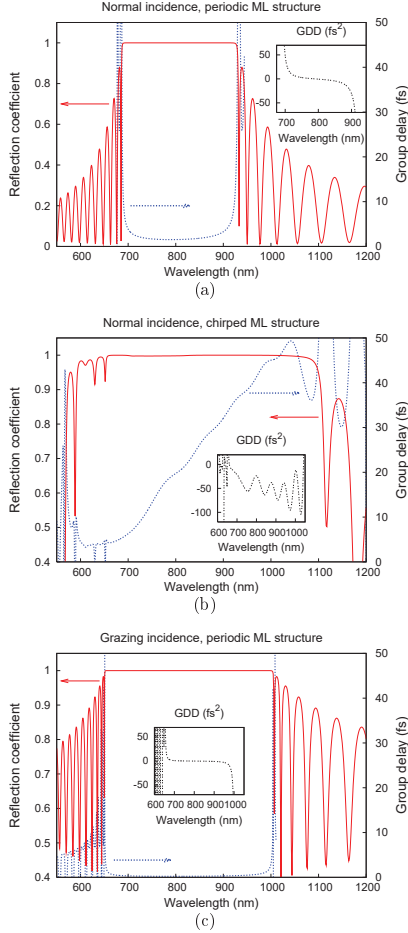
Figure 2.3: (a) Reflectivity and group delay as a function of wavelength for a periodic multilayer structure designed for normal incidence, (b) for a chirped ML structure designed for normal incidence and (c) for a periodic ML structure designed for grazing incidence, S-polarization. Group delay dispersion vs wavelength functions are shown in the insets.

2.2.3   Applications

The above discussions show that periodic grazing incidence mirrors could be an alternative of chirped mirrors in broadband or broadly tunable ultrafast lasers. For example, femtosecond pulse optical parametric oscillators could be based on such mirrors in a ring oscillator arrangement [17]. In this case it is necessary that mirrors are designed for a certain angle of incidence that add up to 360°. For instance, the above described 80° mirrors would require an 18-mirror setup. Another possible application of grazing incidence dielectric mirrors could be their use in ring oscillators based on the micro-disk analogy [18].

It has to be pointed out, that the advantage of considering grazing incidence periodic mirrors as an alternative of normal incidence chirped mirrors is not only their low and smooth dispersion profile but also the ease of their design and manufacturing.
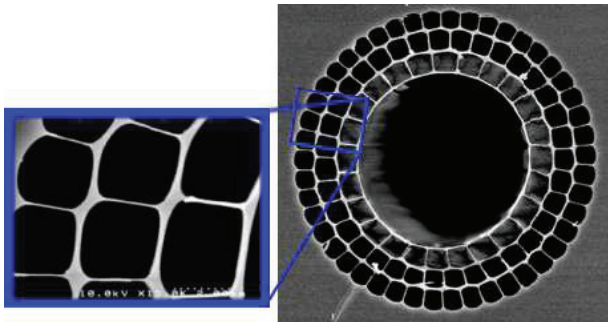
Figure 2.4: Scanning electron microscope image of the cross-section of a hollow-core Bragg photonic bandgap fiber [21].

2.3 Design of HC Bragg PBFs

2.3.1 Introduction

Another field of optics where grazing incidence dielectric structures are used is that of photonic bandgap fibers, especially all-silica hollow-core photonic bandgap fibers, in which the light is guided in air in order to avoid nonlinear effects [19, 20]. These fibers exhibit anomalous dispersion in most of the bandgap that makes them an attractive candidate for dispersion compensation in all-fiber setups. In the present work, our primary goal was to solve the problem of the so-called "leaking modes" that could be responsible for resonant losses in HC PBFs, namely in HC all-silica Bragg PBFs [21]. These fibers can be considered as Bragg fibers [4] because of their nearly cylindrical symmetry that contains concentric layers of silica and air. Deviation from the ideal structure is caused by the silica struts that are necessary to set the spacing between the silica layers, see Fig. 2.4. Attempts to eliminate leaking modes have − to our knowledge − only been done by numerical models, investigating the effects of different structural parameters by manual optimization [22], until now.

We found that two kinds of loss mechanisms can be distinguished for HC Bragg PBFs. While leaking modes are due to the high standing wave field in the air spacer layers and can be removed by correct design of the structure (see optimization e.g. [22]), "surface modes" still appear in the silica struts due to symmetry concerns and can only be described by complicated full-vectorial models [23, 24]. We realised that leaking modes originate in the index rising effect of the silica struts, that in-

crease the effective refractive index of the air cladding regions above unity, and this few percent change calls for considerable modification of the optimal layer thickness values. By proper design, however, the mode anti-crossing events (that cause leaking loss and segment the bandgap to many smaller ones) can be avoided and thus structures exhibiting an ultrabroad bandgap can be constructed.

2.3.2 Analysis of leaking modes in HC Bragg PBFs

As an approximation, photonic bandgap fibers can be regarded as 2D dielectric high reflectors, in which light propagates at grazing incidence. The critical angle of incidence, Θ_0, can be derived from the real part ($\Re$) of the effective refractive index $n_{\text{eff}}(\lambda)$ of the fiber structure using Eq. (2.12). We must note that the critical angle of incidence is the lowest value of incident angle for which the light is guided. A PBF designed for this value of angle of incidence will result in a bandgap shifted towards the longer wavelengths compared to the case when the design is optimized for the mean value of the incident angle. This fact explains the wavelength mismatch between the 1D and FEM calculations shown in the last section (see Fig. 2.9 (a) and (b)).

$$\Theta_0 = \arcsin(\Re(n_{\text{eff}})). \tag{2.12}$$

Similarly to standard quarter-wave dielectric high reflectors, in order to obtain resonance free, i.e. leaking mode free designs physical thicknesses (PT_i) of the cladding layers (i) should meet the $\lambda/4$ condition designed for oblique angle of incidence and λ_0 central wavelength:

$$\text{PT}_i = \frac{\lambda_0}{4} \frac{1}{n_i \cos(\Theta_i)}, \tag{2.13}$$

where n_i are the refractive indices of the different layers and Θ_i are the refraction angles, which values are calculated by Snell's law.

During investigations on HC Bragg PBFs, we found that the effect of this equation is striking. HC Bragg PBFs consist of silica and air layers serving as the high and low index layers, respectively. To set the spacing between the silica layers, silica struts (support bridges) are added. As we realized, the few percent change in the refractive index caused by the support bridges in the air layers dramatically changes physical layer thickness of the corresponding air layer that meets the quarter-wave condition. As our following simulation results show, neglecting this slight modification of the effective refractive index results in interface-mode anti-crossing events

which segment the bandgap to many smaller ones and dramatically reduce the usable bandwidth. However, choosing the physical layer thicknesses properly, we can easily eliminate these leaking modes. In our simulations, the index-rising effect of the support bridges (thickness ~ 50 nm to design a physically realizable fiber) was first estimated to be ~ 0.02, resulting in a low index layer (n_L) of 1.02. It has to be mentioned that this value is just an upper estimate for the index rising effect, that we considered, practically $n_L \approx 1.005$ was calculated on the basis of geometrical silica fraction in the air spacer layer as discussed in Section 2.3.4. The physics behind the sensitivity to n_L and the angle of incidence in terms of refraction angle and thus physical thickness of a quarter-wave layer that has a refractive index very close to unity is similar to the mirage effect at grazing incidence of light [25].

First of all, we investigate the effect of the silica struts on the physical thickness values of the air spacer layers using Eq. (2.13) as the function of the "effective refractive index" of the low index layer, that is slightly higher than 1 (see Fig. 2.5 (a)). In case of infinitely thin silica struts ($n_L = 1.0$), the spacing between the concentric fused silica rings has to be set to 3.6 µm in order to meet the quarter-wave condition at our desired central wavelength (1 µm) of the bandgap. It has to be pointed out that this thickness value also depends on the angle of incidence. We have chosen this parameter to be $86°$ for our calculations according to our FEM simulation results (see later). Since the effective index of dielectric waveguides such as our HC Bragg PBFs slightly varies with the wavelength (dispersion), the angle of incidence should be recalculated at each wavelength. We found, however, that this effect does not affect considerably the width of the bandgap, and it does not result in new leaking modes harming the bandgap. For $n_L \approx 1.02$, the spacing between the fused silica rings has to be reduced considerably: the optimal spacing resulting in the widest bandgap at around 1 µm is ~ 1.2 µm (note for the modification of the refraction angle in this cladding layer). Evidently, neglecting the small index rising effect of the fused silica struts during the design of such structures results in higher order bandgaps or leaking modes at around the center of the bandgap. Increase in the thickness of support bridges calls for further reduction in the spacing of the fused silica rings, but this change is not so dramatic when the thickness is higher ($n_L > 1.02$).

Another striking effect of the support bridges is demonstrated in the same figure (Fig. 2.5 (a), right axis): in spite of the minor modification in the effective refractive index of the air spacer layers (from $n_L = 1.0$ to $n_L = 1.02$), the available maximum bandwidth ($\Delta\omega$) is considerably reduced from > 1.7 fs^{-1} to 1.2 fs^{-1} at around 1 µm, when the physical thickness values of the air spacer layers are properly set to meet
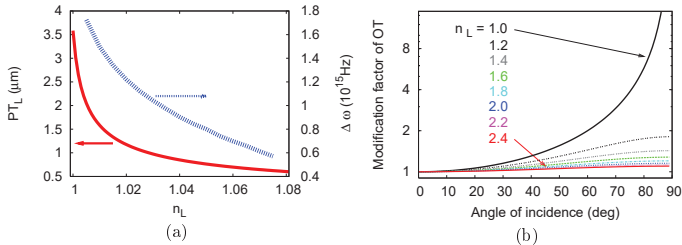
Figure 2.5: (a) Computed physical thickness of the low index layer (PT_L) as a function of the layer index (n_L) when meeting the $\lambda/4$ condition at an angle of incidence $\Theta_0 = 86°$, and computed bandwidth ($\Delta\omega$) of the bandgap as a function of n_L when $n_H = 1.45$ (P polarized light). (b) Computed modification factor of the optical thickness of different refractive index layers as a function of the incident angle.

the quarter-wave condition requirement. This is in agreement with the results in Section 2.2.

In case of hollow-core fibers the modification factor of the optical thickness (OT) by the cosine of the angle of incidence ($1/\cos(\Theta_L)$) is shown in Fig. 2.5 (b). As the angle of incidence increases, the optical thickness fulfilling the quarter-wave condition gets higher. However, this effect gets extremely high as the refractive index of the low index layer approaches 1 (note for the logarithmic scale in the figure) which is the case of support bridges used in HC Bragg PBFs, and analogous to the appearance of mirages close to the horizon.

Our present investigations suggest that in order to preserve high bandwidth of hollow-core all-silica Bragg fibers, designs comprising a small number of very thin fused silica struts should be preferred. In the following studies, we use 12 pieces of support bridges in the spacer layers and their thickness is chosen to be 50 nm which is realistic to be manufactured.

2.3.3 One-dimensional simulations of HC Bragg PBFs

Our aim was to design a structure consisting of 3 silica-air layers which support band-gap guidance around 1 µm without the leaking modes. It is known that the leaking modes appear in the band-gap due to the support bridges in the air layers which cause a small refractive index increase. That leads to phase changes by the increased optical path length in the air layers. Until now attemps on solving this problem were by changing layer thicknesses in small steps creating transmission

maps calculated by FEM which is very time-consuming and ineffective in designing HC fibers.

Our structure consists of a 6 µm core and alternating layers of silica with thickness d_i and of air with thickness L_i, $i = 1, 2, 3$ (see Figure 2.6). The physical thicknesses of the layers should be chosen according to the relevant phaseshifts.
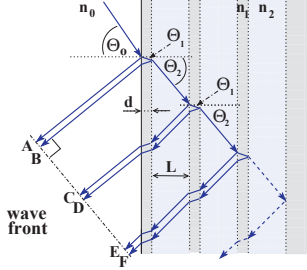

Figure 2.6: Structure of the cladding

2.3.4 Results of the one- and two-dimensional simulations of HC Bragg PBFs

In our numerical examples, designs comprising 3 silica-air layer pairs are presented (see Fig. 2.7 (a), and Fig. 2.7 (b) for a 1D equivalent and the 2D fiber structure, respectively) which support bandgap guidance around 1 µm.

In order to estimate the index rising effect of the silica struts reasonably we applied an approximate formula (Eq. (2.15)) for the air layer thicknesses instead of Eq. (2.13) that takes the silica filling fraction of the given layers into account.

The formula can be deduced by considering that for grazing incidence, Θ_0 and Θ_i have large values, $\alpha = \pi/2 - \Theta$ is small and thus $\cos(\alpha) = \sqrt{1 - \sin^2(\alpha)} \approx 1 - \sin^2(\alpha)/2$. From Snell's law we obtain the following:

$$\sin^2 \alpha_i = \frac{\sin^2 \alpha_0 + 2(n_i - 1)}{n_i} \tag{2.14}$$

For the index difference in layer i we might substitute $n_i - 1 = \mathrm{SFF}_i \cdot (n_s - 1)$ where n_s is the refractive index of silica and SFF_i is the silica filling fraction of layer i according to its cross-sectional geometrical fraction. The approximate formula for the physical layer thicknesses obtained from Eq. (2.13), Eq. (2.14) and $\cos(\Theta_i) = \sin(\alpha_i)$ is:

$$\mathrm{PT}'_i = \frac{\lambda_0}{4} \frac{1}{\sqrt{n_i}} \frac{1}{\sqrt{\cos^2 \Theta_0 + 2\mathrm{SFF}_i \cdot (n_s - 1)}}, \tag{2.15}$$
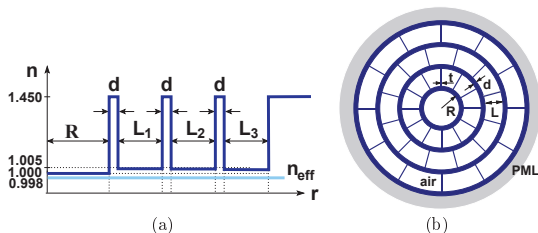
Figure 2.7: (a) Refractive index (n) profile of the 1D equivalent of the fiber, with respect to the distance from the center of the fiber (r). The obtained effective refractive index of the cladding structure is shown with a light blue line. (b) Cross-section of the HC Bragg PBF used in our FEM simulations.

where it is to be pointed out that both quantities in the square root in the last denominator are small values causing the main modification on the layer thickness.

After an initial guess for the refractive indices of air layers ($n_L = 1.02$), the Θ_i values and thus the corresponding fiber structure (PT_i) are calculated. From the obtained structure the silica filling fractions of the air spacer layers are calculated which values are further used to calculate the physical thicknesses of the layers by Eq. (2.15). After a few steps of iterating the PT'_i and SFF_i values we obtain a fiber structure that exhibits an even wider bandgap than that of the initial guess.

1D simulation results are shown in Fig. 2.8 and the reflection curves, corresponding to the transmission of the fiber are summarized in 2.9 (a). The ideal design in which the support bridges in the air spacer layers − and thus the index-rising effect − are neglected exhibits a very wide bandgap. The reflection and dispersion are shown in Fig. 2.8 (a) (and the transmission of such idealistic fiber is plotted with black dashed line in Fig. 2.9). Here, $n_L = 1.00$, $PT_L = \lambda_0/4/\cos(\Theta_0) = 3.584$ µm, $n_H = 1.45$, $PT_H = \lambda_0/4/n_H/\cos(\Theta_H) = 0.237$ µm, $\Theta_0 = 86°$ (corresponding to $n_{eff,0} = 0.9976$, using Eq. (2.12)). The relative phases in different positions of the phasefront contributing to the partial waves reflected from the different surfaces are calculated at three different wavelength values. At the central wavelength the partial waves are exactly in phase and at other wavelength values the relative phaseshift between them is a constant, as it is expected. The relative phase shifts are plotted in Fig. 2.8 (b). When the small index-rising effect of silica struts is taken into account but the spacer thickness is not corrected for it ($n_L = 1.02$ and $PT_L = 3.584$ µm), leaking modes destroy the bandgap. It is to be noted that from the practical point of view the problem is only partially caused by the narrow
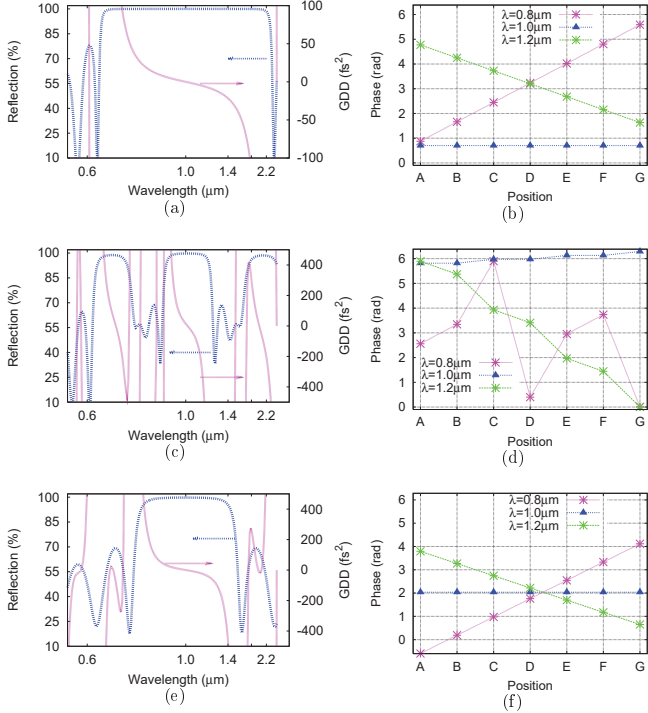
Figure 2.8: Computed reflection and corresponding group-delay dispersion as a function of wavelength for photonic bandgap structures of the following designs: (a) $n_L = 1.00$ and $PT_L = \lambda_o/4/\cos(\Theta_0) = 3.584$ µm exhibiting a very wide band-gap, (c) $n_L = 1.02$ and $d_L = 3.584$ µm with the leaking modes destroying the band-gap, (e) $n_L = 1.02$ and $d_L = \lambda_o/4/1.02/\cos(\Theta_2) = 1.175$ µm restoring the band-gap to some degree. (b),(d) and (f) are the relative phases in different positions of a wavefront contributing to the partial waves reflected from the different surfaces at three different wavelength values, see Fig. 2.6.

bandgap. The other problem is the dispersion curve which is extremely varying even inside of the reduced bandgap regions. This can be observed in Fig. 2.8 (c) (blue dotted line in Fig. 2.9). The origin of the resonances lies in the relative phase shifts, shown in Fig. 2.8 (d). There is a small variation in the phases at 1 µm, and it becomes extremely large as moving to further frequencies (at 0.8 µm the variation is significantly higher than at 1.2 µm). This is the reason why these curves

are plotted with the wavelength axis equidistant in frequency values. The corrected quarter-wave design ($n_L = 1.02$ and $PT_L = \lambda_0/4/1.02/\cos(\Theta_L) = 1.175$ µm) exhibits a broad bandgap free of leaking modes (see Fig. 2.8 (e), and red solid line in Fig. 2.9), however, the bandwidth is reduced compared to the ideal case, in agreement with Fig. 2.5 (a). The phase relation is restored as well (see Fig. 2.8 (f)) to similar characteristics as it was to be seen in Fig. 2.8 (a). Furthermore, the approximate quarter-wave design with iteration parameters for the structure ($n_{L1} = 1.006, n_{L2} = 1.005, n_{L3} = 1.0042$, $PT'_{L1} = 1.922$ µm, $PT'_{L2} = 2.051$ µm, $PT'_{L3} = 2.159$ µm) further broadens the bandgap implying the necessity for estimating n_{Li} appropriately (green line in Fig. 2.9, "iterated structure").
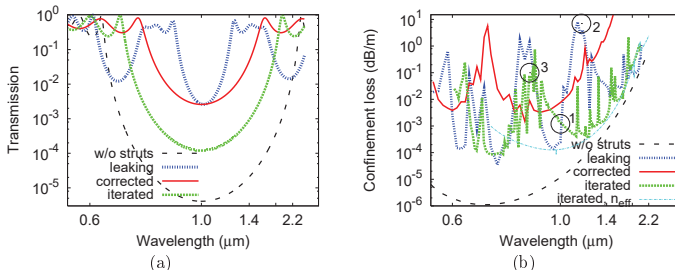

Figure 2.9: (a) 1D computation results for transmission of the multilayer structure (corresponding to the loss of the fiber) as a function of wavelength for structures of the following designs: $n_L = 1.00$ and $PT_L = 3.58$ µm ideal structure without silica struts (black dashed line), $n_L = 1.02$ and $PT_L = 3.58$ µm leaking modes (blue dotted line), $n_L = 1.02$ and $PT_L = 1.18$ µm corrected $\lambda/4$ structure (red solid line), $n_{Li} = 1.006, 1.005, 1.004$ and $PT_{Li} = 1.92, 2.05, 2.16$ µm, respectively: iterated chirped structure (green solid line) and (b) corresponding FEM results including the homogenized iterated chirped structure with $n_{eff,i}$ values instead of the silica struts (light blue narrow dash dotted line). Points in the graph marked with circles refer to different mode field distributions shown in Fig. 2.10.

Corresponding FEM calculation results are shown in Fig. 2.9 (b). The FEM simulation was carried out on a fiber structure consisting of a 6 µm core (R), 3 alternating layers of silica and air (with layer thickness d and L, respectively), and 12 silica struts of 50 nm thickness (t) in each air layer (see Fig. 2.7 (b)) except for the ideal case when silica struts are neglected (dashed line). The properly designed structure (red solid line) is free of "leaking modes" (compare to blue dotted line), however some perturbation due to still existing "surface modes" can be observed. The iterated structure (green dotted line), that normally further broadens the bandgap

has – in our case – significant surface modes that segment the bandgap to narrower transmission windows. The comparison with the same iterated structure but of cylindrical symmetry is shown by a narrow dash dotted blue line in which the air spacer layers with silica struts are replaced by the corresponding $n_{\mathrm{eff},i}$ values. This comparison shows that the 1D simulation results are in agreement with the 2D FEM results in case of fibers with cylindrical symmetry, and that the significant loss peaks in this case are due to surface modes caused by the symmetry breaking in contrast to leaking modes that are due to the incorrect design. The difference between the two loss mechanisms can also be observed on the mode distributions calculated by FEM. For comparison, typical mode distributions are shown in Fig. 2.10 for the fundamental mode (a), the leaking mode with increased field between the silica layers (b), and the surface mode with the field concentrating in the silica struts (c). The fundamental mode was calculated at 1000 nm wavelength on the iterated structure, corresponding to the green curve in Fig. 2.9, the leaking mode was calculated at 1150 nm, on the "leaking structure", corresponding to the blue curve in Fig. 2.9 and the surface mode was calculated at 838 nm, on the iterated structure corresponding to the green curve, as well.

It is to be mentioned that the correct homogenization of the silica struts should be done according to the volume average of the $\varepsilon|E|^2$ for the fundamental mode. The effective refractive indices of the low index layers would be in this case $n_{\mathrm{L1}} = 1.0146$, $n_{\mathrm{L2}} = 1.0115$ and $n_{\mathrm{L3}} = 1.0123$ (corresponding to Fig. 2.10 (a)). The elevated indices compared to the ones calculated from the silica filling factors are due to the fact that the electromagnetic field has an inhomogeneous distribution, and it is slightly concentrated around the silica struts.
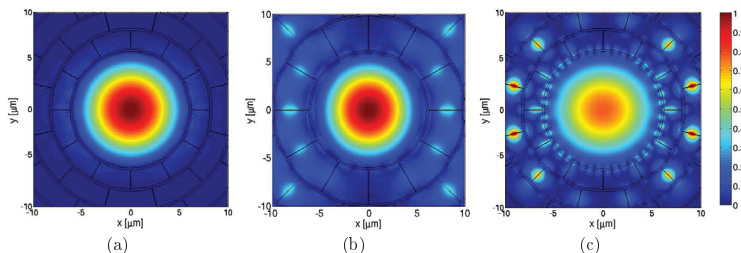

(a) (b) (c)

Figure 2.10: Mode distributions of the (a) fundamental mode (corresponding to point 1 in Fig. 2.9 (b)), (b) leaking mode (corresponding to point 2 in Fig. 2.9 (b)) and (c) surface mode (corresponding to point 3 in Fig. 2.9 (b), green line)

2.4 Conclusion

We have investigated amplitude and phase behavior on reflection of PB dielectric structures used at grazing incidence of light. Results on the 1D structures show that such designs could be advantageous in laser systems where high reflectivity and nearly uniform dispersion is required over a wide wavelength range. For instance, grazing incidence dielectric mirrors can be well applied for broadband feedback in ultrabroadband or broadly tunable ultrashort pulse lasers and optical parametric oscillators.

Based on the 1D model, we have extended our investigations to 2D PB structures such as PBFs. During our studies we found that the time consuming FEM and the simple 1D thin-film analysis provide similar results when the input parameters (such as angle of incidence) for the latter method are properly chosen. The most important consequences of our simulations are obtained for HC Bragg PBFs: we found that a few percent modification of the refractive index ($\leq$ 2%) due to silica support bridges may cause dramatic change in the usable width of the bandgap in these fibers. Therefore, during the design an accurate "average" refractive index has to be taken into account for the cladding layers of HC Bragg PBFs in order to meet the well known quarter-wave condition. When this condition is satisfied, HC Bragg PBFs can provide a relatively wide and leaking mode free bandgap with anomalous dispersion over most of the bandgap. Due to their engineerable dispersion, we regard them as promising tools for broadband intra- or extra-cavity dispersion control in femtosecond pulse fiber lasers and amplifiers [26]. Finally, we note that the design procedure described in this chapter can be applied for giving estimate solutions in the design of all kinds of photonic bandgap fibers, as well.

3 Pulse compression by the use of a highly nonlinear photonic crystal fiber

In this chapter compression of sub-nanojoule laser pulses using the spectral broadening in a commercially available, highly nonlinear photonic crystal fiber (PCF) is discussed. A two-fold compression of nearly transform limited, 24 fs seed pulses of a Ti:sapphire oscillator is experimentally demonstrated [T2]. The motivation is given in Section 3.1. It is followed by some theoretical considerations in Section 3.2, that assist to the Nonlinear Schrödinger-equation, introduced as the fundamental equation determining pulse propagation in optical fibers, described in Section 1.1. The experiment and its results are described in Section 3.3, and the conclusion is drawn in Section 3.4.

3.1 Motivation

Pulse compression of optical pulses down to 5 fs were demonstrated in a wide variety of experimental arrangements using standard single mode optical fiber [27] or gas-filled hollow-core fiber as a nonlinear medium [28]. The common feature of previous studies in this time domain is that they require laser pulses at energy levels well above 10 nJ, i.e. pulse energies that are difficult to obtain directly from a femtosecond pulse laser oscillator. As a result of recent development of small core diameter, single mode photonic crystal fibers, tenfold pulse compression was demonstrated in a few experiments [29, 30] at nJ or sub-nJ pulse energies. These resulted in typical compressed pulse durations of 20 to 35 fs. Recently, the possibility of compressing supercontinuum generated in a 5 mm long micro-structured fiber was also reported [31]. In this latter experiment, 2.7 nJ, 15 fs transform limited pulses obtained from a low repetition rate Ti:sapphire oscillator were compressed to 5.5 fs using an adaptive compression technique based on spectral-phase interferometry for direct electric field reconstruction (SPIDER).

In [T2], it was theoretically shown that it is possible to obtain compressed sub–6 fs pulses using nanojoule or sub-nanojoule seed pulses around 800 nm by utilizing only a small-core area PCF and prism-pair / chirped mirror compressors. In a previous study [29], it was shown that the compressed pulse duration was primarily limited by the maximum available wavelength difference between the laser central wavelength (750 nm) and the zero dispersion wavelength (767 nm) of the PCF sample. Novel PCFs with red-shifted zero dispersion wavelengths, however, can improve both the quality and the duration of the compressed pulses when the input and output chirp compensation parameters are chosen properly. It is worth pointing out that 1 nJ seed pulse energies with the required pulse durations can be obtained easily from low pump threshold, mode-locked Ti:sapphire laser oscillators pumped by only 1.2 W at 532 nm [32].

In the experiment described below (Section 3.3) the pulse energy is < 1 nJ, which does not result in considerable spectral broadening in standard single mode-fibers. Nonlinear spectral broadening is achieved in a small core area PCF which allows the reduction of pulse duration. The proper input and output chirp compensation was simulated and optimized by Z. Várallyay based on the theory to be read in Section 3.2.

3.2 Theory

The pulse propagation through PCFs is described by the Nonlinear Schrödinger-equation, Eq. (1.8), Section 1.1. The input pulses used in the simulation exhibit a sech^2 spectral intensity function and sech^2 temporal intensity envelope function that is typical for femtosecond solid state laser oscillators. We used a highly nonlinear PCF (type "2.2 Nonlinear PCF", Crystal Fibre [33], see Fig. 3.1 for the cross-section) with 2.2 µm core diameter to induce spectral broadening of the pulse. The dispersion data of the PCF, required for the simulations were provided by the manufacturer in a limited spectral range, so it was further approximated by a Taylor-expansion:

$$D(\lambda) = D_0 + S(\lambda - \lambda_0) + \frac{T}{2}(\lambda - \lambda_0)^2 + \frac{F}{6}(\lambda - \lambda_0)^3. \tag{3.1}$$

In Eq. (3.1), λ_0 is the central wavelength of the seed pulse, D_0 is the dispersion at the central wavelength, S is the dispersion-slope, T is the third-order dispersion [6] and F is the fourth-order dispersion, with the corresponding values of $D_0 = -27.15 \cdot 10^{-6}$ s/m^2, S= $0.51772 \cdot 10^3$ s/m^3, T= $-3.277854 \cdot 10^9$ s/m^4, F= $1.642713 \cdot 10^{16}$ s/m^5, respectively.

We found that the compression level strongly depends on the initial chirp of the pulse injected into the fiber for pulses that have transform-limited durations in the sub-100 fs regime. This is in agreement with previous studies [29, T2.1]. Providing a small linear pre-chirp results in less efficient spectral broadening, thus the pulse duration becomes slightly longer. However, this may result in lower distortion during propagation in the fiber as the distortion is due to the strong third-order dispersion (TOD, or here $\sim$S) of the PCF. The spectral broadening can be controlled at a certain energy level in this way, and thus frequency components can be avoided that may harm the quality of the compressed pulses.

3.3 Experiment and results

Our Ti:sapphire laser oscillator (FemtoRose 20 MDC [34]) operated at 797 nm with $\sim$24 nm bandwidth, and delivered 24 fs sech^2 pulses at a repetition rate of 76 MHz. A PCF piece of length of 22 mm was the shortest that could be cut with our fiber cleaver, although the optimal length predicted by the simulation was shorter. Accordingly, the input pulse energy had to be reduced in order to get spectral shapes similar to what can be obtained with a 6 mm long PCF used in the simulations. The experimental setup is shown in Fig. 3.2. After the laser a Faraday isolator

---

[6]Note for the difference of the expansion of the propagation constant into a Taylor-series with respect to frequency in Section 1.1, Eq. 1.10. Here, the dispersion coefficients are defined according to the expansion with respect to wavelength.

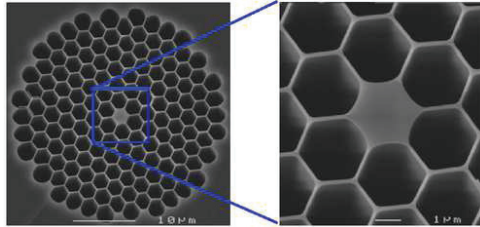Figure 3.1: SEM images of the highly nonlinear photonic crystal fiber cross-section [33].
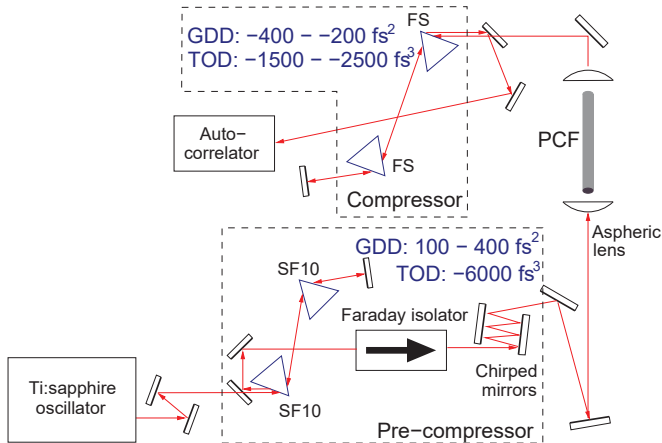

Figure 3.2: Experimental setup. An SF10 prism pair in combination with chirped mirrors are used for pre-compression of a 24 fs pulse with central wavelength of 797 nm. The spectrally broadened pulse exiting the PCF is compressed by a fused silica (FS) prism pair / chirped mirror compressor resulting in a two-fold temporal compression.
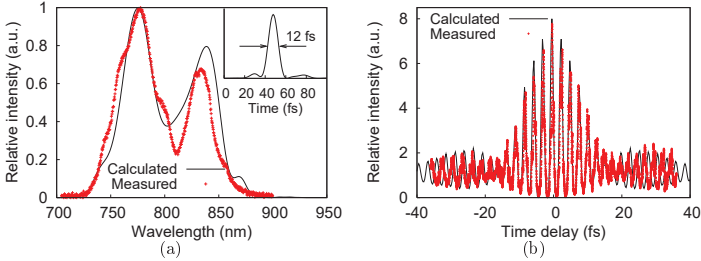
Figure 3.3: (a) Measured and computed spectra with the retrieved compressed pulse shape in the inset. (b) Corresponding autocorrelation traces. Input pulse parameters for the calculation: $E_0 = 0.6$ nJ, FWHM = 24 fs, $GDD_{in} = 400$ fs^2, $TOD_{in} = -6000$ fs^3, $L_{PCF} = 22$ mm. Output dispersion compensation parameters: $GDD_{out} = -320$ fs^2, $TOD_{out} = -2000$ fs^3.

was installed to avoid feedback from the fiber. In order to provide the optimal pre-chirp parameters, a pre-compressor was built in which the positive dispersion introduced by the isolator (GDD ≈ 2700 fs^2) had to be compensated as well. The pre-compressor comprised an SF10 prism pair introducing negative GDD and TOD and a pair of chirped mirrors that compensated the TOD by introducing negative GDD but positive TOD. By this arrangement we could set the second order pre-chirp (GDD_{in}) between 100 fs^2 and 400 fs^2 and the third order to $TOD_{in} \approx -6000$ fs^3.

After fitting the simulation results to the measured spectra, see Fig. 3.3 (a), the parameters for dispersion compensation at the output of the fiber were estimated. We obtained two-fold compression for the 24 fs pulses with $GDD_{out} = -400$ fs^2 to -200 fs^2 and $TOD_{out} = -1500$ fs^3 to -2500 fs^3. The dispersion compensation was carried out by a fused silica prism pair. The measured and computed autocorrelation traces are shown in Fig. 3.3 (b). The inset of Fig. 3.3 (a) shows the retrieved temporal pulse shape by the simulation, with an FWHM pulse duration of 12 fs.

3.4 Conclusion

We have demonstrated that it is feasible to compress the initially transform limited pulses by a non-dynamic compression technique, using a commercially available photonic crystal fiber and a cost effective, low pump threshold ($P_{\text{pump}} \approx 1.2$ W) Ti:sapphire laser with ~ 1 nJ pulse energy. Experimentally, the initially ~ 24 fs pulses were compressed to ~ 12 fs pulse duration in a 22 mm fiber piece, that was the shortest piece of fiber we could cut. Theoretically it was shown, that by the optimization of input and output chirp parameters, high quality, sub-6 fs pulses could be generated by using an even shorter fiber piece. Further reduction of the compressed pulse duration at such energy levels is possible by application of new PCFs with red-shifted zero-dispersion wavelengths and lower third-order dispersion values.

4 Design of a passively mode-locked all-fiber, all-normal dispersion ytterbium ring oscillator

In this chapter the development of a passively mode-locked all-fiber ytterbium ring oscillator is reported [T3]. The laser characteristics were investigated and compared in specific positions of the resonator, in order to characterize the pulse shaping mechanism and obtain the optimal position for the output port for different applications. It was found that the laser operates in the "all-normal dispersion" mode-locking regime, and the pulse-shaping is based on nonlinear polarization evolution in the fiber sections together with spectral and temporal filtering by a polarizing element. The oscillator produces relatively high quality pulses, externally compressible to as short as 195 fs.

In Section 4.1 and 4.2 the motivation and an overview of mode-locked fiber lasers are given based on literature [35, 36, 37]. Theory described in Section 1.4 and the references are aimed to help further understanding.

4.1 Motivation

Generation of ultrashort laser pulses is conventionally done by solid-state mode-locked lasers utilizing bulk optics including the gain materials (e.g. Ti:sapphire, Nd-glass), laser mirrors etc. These lasers require stable laboratory-like environment with reduced variance in temperature and vibrations, and 1-2 m of space on an optical table. They are usually highly power consuming, and also require precise adjustment for the maintenance of stable mode-locked operation.

In the past few years passively mode-locked fiber lasers have gained high interest because of their potentially compact, environmentally stable and alignment-free design combined with high quality spatial mode-field distribution. The key advance in the development of fiber lasers was the discovery of rare-earth doped fibers as the laser gain media because of their high saturation fluence, broad gain bandwidth, and the excellent heat dissipation. The high saturation fluence allows very efficient pumping − which might reach 80%, − and the broad gain bandwidth supports ultrashort pulses, as short as 30 fs in the case of ytterbium.

The development of fiber lasers has initially been driven by applications in telecommunication and by scientific investigations by nonlinear microscopy. The doping material of the gain fiber in these lasers is erbium (Er), emitting at 1.55 µm wavelength, and neodymium (Nd), operating around 1 µm, respectively. Recently, ytterbium (Yb) has attracted much attention as a gain medium around 1 µm because it offers many advantageous spectroscopic properties, including high quantum efficiency, absence of ground-state and excited-state absorptions, long upper-state lifetime, and broad gain spectrum. Furthermore, Yb can be directly optically pumped at 915 and 980 nm by laser diodes. As a result, Yb-doped fibers are likely to supersede fibers with other doping materials emitting around 1 µm.

Furthermore, with the technological development of high power diode lasers and of double clad large mode area fiber amplifiers, high average power fiber lasers give a comparable performance to classical solid-state lasers, even though, in terms of reliability and long term stability the latter are still preferred in comparison with fiber lasers.

Our motivation was to create a compact and easily alignable, environmentally stable fiber source at 1 µm, that produces $\sim$ 300 fs pulses, capable of practical application. Expectations included high signal-to-noise (S/N) ratio, possibly unmodulated spectrum for reasonable amplification, and the fiber optical components being commercially available.

4.2 Overview of passively mode-locked ytterbium fiber lasers

The pulse formation process in passively mode-locked fiber lasers is complex, and is rather difficult to explain in general. As an introduction, the *Modes of operation in a fiber laser* are described in context with pulse formation. Different modes of operation could be observed in our fiber laser by changing the state of polarization at some point in the resonator. Measurement results are demonstrated in Section 4.2.1 to show the characteristics of the different modes.

Several mechanisms can be distinguished that lead to the formation of stable pulse trains. The mechanisms correspond to different parameter ranges, such as net-cavity dispersion or nonlinearity, and they determine the evolving pulse characteristics. These *Mode-locking regimes* of fiber lasers are briefly overviewed in Section 4.2.2. After that, the principles of *Mode-locking by nonlinear polarization rotation* (NPR) are described in more detail in Section 4.2.3, as this is an important phenomenon, contributing to the mode-locking mechanism in our fiber laser. Finally, premise and some considerations of the *Construction of mode-locked fiber lasers* are discussed in Section 4.2.4 which gave the direction of the development of our setup.

The initiation of pulse formation in fiber lasers is provided by temporal fluctuations induced by spontaneous emission in the doped fiber. Fluctuations are filtered by a saturable absorber (e.g. a Bragg-reflector or NPR with a polarizer) and the signal is enhanced by gain during multiple round-trips in the laser cavity. This process continues until an intense pulse (or intense multiple pulses) capable of saturating the absorber is formed, otherwise no stable solutions emerge. The pulse is stabilized when the parameters affecting its evolution are in balance, and the temporal and spectral shapes are exactly reproduced after one round-trip in the resonator. Spectral broadening is determined by gain and nonlinearity in the fiber and it is compensated by spectral filtering by some kind of a filter or the limited bandwidth of gain. In some cases, i.e., in soliton lasers, spectral broadening induced by positive nonlinear phaseshift is compensated by anomalous dispersion. The temporal evolution is influenced by dispersion and filtering[7]. It has to be noted, that the effect of dispersion is dependent on the spectral width. For highly chirped pulses, filtering by a spectral filter and self-amplitude modulation by the saturable absorber might act on both of the temporal and spectral profiles.

---

[7]either temporal filtering by a saturable absorber, on the basis of self-amplitude modulation, or through spectral filtering of the chirped pulse

4.2.1 Modes of operation in a fiber laser

Lasers operate simultaneously in a large number of longitudinal modes falling within the gain bandwidth. The frequency spacing among the modes is given by $\Delta\nu = c/L_{\text{cav}}$, where L_{cav} is the optical length of the cavity. If all modes operate independently of each other, with no definite phase relationship among them, the interference terms in the total intensity $|E(t)|^2$ average out to zero. This is the situation in multi-mode *continuous wave* (cw) lasers.

Mode-locking occurs when phases of various longitudinal modes are synchronized such that the phase difference between any two neighboring modes is locked to a constant value. Locking of such phase relations enables a periodic variation in the laser output which is stable over time, and with a periodicity given by the round-trip time of the cavity. A stable pulse train captured by a photo-detector is shown in Fig. 4.1 (a). If sufficiently many longitudinal modes are locked together with only small phase differences between the individual modes, it results in a short pulse which may have a significantly larger peak power than the average power of the laser. The origin of mode-locking is best understood in the time domain. A laser in steady-state is a feedback system, where the gain per round-trip is balanced by the losses. If a nonlinear element is inserted in the cavity, which introduces a higher loss at lower powers, the laser may favor a superposition of longitudinal modes corresponding to a short pulse with high peak power. This nonlinear element is referred to as a saturable absorber. However, a further requirement for obtaining stable mode-locking is that the pulse reproduces itself after one round-trip (within a total phaseshift on all the longitudinal modes). The phase relations between different modes are affected by dispersion, gain bandwidth, nonlinear phase shifts etc. Although an infinite number of different pulses could be constructed as different superpositions of longitudinal modes, usually only a single pulse [8] is a stable solution of the cavity, and thus the output pulse characteristics can be designed and controlled by changing the physical parameters of the comprising laser elements.

Another mechanism used for the generation of short, typically ns duration (and low repetition rate) optical pulses is Q-switching. It is achieved by inserting some type of a variable attenuator inside the laser resonator. This might be for example an output coupler that couples light out of the resonator periodically in time (e.g. electro- or acousto-optic modulator). When the attenuator is functioning, the light exiting the gain medium does not circulate, and lasing cannot begin. This attenuation inside the cavity corresponds to a decrease in the quality factor (Q-

---

[8] determined by the lowest loss

factor) of the optical resonator. A high Q-factor corresponds to low resonator losses per round-trip, and vice versa. When Q-switching is present simultaneously in a mode-locked laser, however, it leads to a disturbed mode of operation, where the mode-locked pulses are modulated on a long, ns to µs timescale. The oscilloscope signal of a typical pulse train can be seen in Fig. 4.1 (b). We refer to this mode of operation as *Q-switched mode-locking*, to distinguish it from *cw mode-locking*, where no additional Q-switching is present.
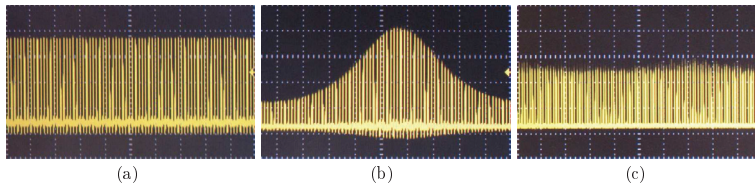

| (a) | (b) | (c) |

Figure 4.1: Oscilloscope signals for different modes of operation in our oscillator: (a) cw mode-locking, (b) Q-switched mode-locked state, and (c) noise-like pulses. The width of the horizontal scale is 1.5 µs.

Lately, another mode of operation was discovered in the field of fiber lasers. *Noise-like pulses* with a broadband spectrum and a short coherence length were first published to have been generated by an erbium-doped fiber laser [38]. The noise-like behavior was observed in the amplitude as well as in the phase of the pulses. The oscilloscope signal of the pulse train can be seen in Fig. 4.1 (c), showing random variation of the amplitude. A theoretical model indicates that this behavior can be explained by the internal birefringence of the laser cavity combined with a nonlinear transmission element and the gain response of the fiber amplifier. For noise-like pulses, the phase distortion caused by the fiber dispersion is relatively weak compared to the initial noise of the pulses and therefore has only a small effect on the coherence. This property is important for optical measurements where coherence plays a fundamental role, such as in autocorrelation measurements. The typical AC function for noise-like pulses has a narrow peak sitting on a wide shoulder, as seen in Fig. 4.2, in comparison with cw mode-locked pulses. The ratio between the peak intensity and the shoulder level of the autocorrelation trace is $\sim 2 : 1$, indicating that the power of the noise-like part of the pulse intensity is similar to the average pulse power. The peak has a duration of the coherence time, while the wide shoulder is not much affected by the chirp of the pulse, as it should be in mode-locked operation. For this reason, the most reliable measurement, whether a

pulse is noise-like or not, is by comparing the autocorrelation functions of a pulse significantly chirped and dechirped, i.e., if the pulse is not compressible, it means, it is noise-like. The inset of Fig. 4.2 shows the compressed pulses after dispersion compensation by a grating pair, by an amount of negative GVD estimated from the spectral and temporal width.

In fiber lasers mode-locked with NPR, it is usually possible to switch between the modes of operation by adjusting the polarization controllers. As observed in [38], for noise-like operation the polarization controllers are set at midrange between maximal and minimal transmissivity of the polarizers for low-power signals.
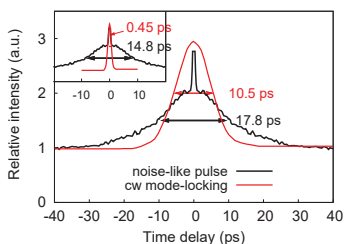

Figure 4.2: Intensity autocorrelation traces for highly chirped cw mode-locked (red), and noise-like pulses (black line). The inset shows the autocorrelation traces after dispersion compensation, by an amount of anomalous dispersion estimated from the spectral and temporal bandwidth. These measurements were carried out on one of our setups similar to the one described in Section 4.3.
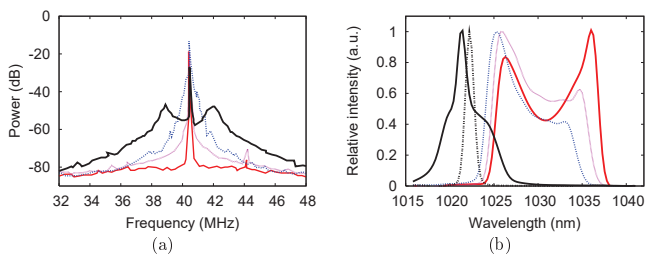

Figure 4.3: (a) RF spectrum and (b) optical spectrum showing the differences in the modes of operation in our ~ 40 MHz laser: cw mode-locking (red), noisy and Q-switched mode-locked state (magenta, blue), noise-like pulses (black line) and cw operation (black dashed line).

The easiest way to observe the different modes of operation is by examining of the radio-frequency (RF) spectrum of the laser (as it is shown in Fig. 4.3 (a)). For cw mode-locking the RF spectrum is a narrow peak at the fundamental repetition rate of the oscillator, and at further harmonics (not shown on this scale). The level of the background is proportional to the power in cw operation. When the polarization controllers are not well adjusted, the noise broadens the peak in the spectrum, leading to noisy and to Q-switched mode-locking at higher noise level. At a certain polarization state, the mode of operation suddenly changes to noise-like operation with side peaks or significant shoulders in the RF spectrum.

In Fig. 4.3 (b) the corresponding optical spectra measured on the PBS output of our laser (see Section 4.4) is plotted. These spectra also show significant difference when varying the modes of operation in the laser.

4.2.2 Mode-locking regimes

Most femtosecond lasers have segments of normal and anomalous GVD, so the cavity consists of a dispersion map. Intra-cavity propagation dynamics is typically characterized by the net-cavity dispersion and by the dispersion map (see Fig. 4.4). For fiber lasers the following regimes are known [39, 7, 40, 41]:
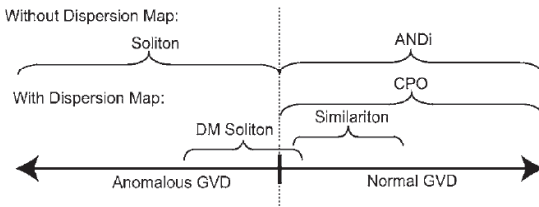

Figure 4.4: Schematics of the main mode-locking regimes of fiber lasers according to the net-cavity dispersion and the existence of a dispersion map [39].

Soliton regime *Soliton mode-locking* is mainly present at negative (anomalous) net-cavity dispersion which compensates for the positive fiber nonlinearity. The temporal as well as spectral shape of a fundamental soliton is secant-hyperbolic (intensity $\sim$ sech^2) with spectral sidebands [9], (see Fig. 4.5 (a)) and little chirp. This

---

[9]Because of the output coupler the soliton energy varies periodically, determined by the cavity length. This creates a nonlinear-index grating which affects soliton properties through Bragg diffraction. The energy lost by the soliton is transformed into dispersive waves, with certain frequencies, which can be resonantly enhanced, causing the sidebands of the soliton spectrum. [42]

regime is well-known for Er-doped fiber lasers [43], where the fiber itself provides anomalous dispersion. The output energies of such lasers are limited to ∼ 0.1 nJ.
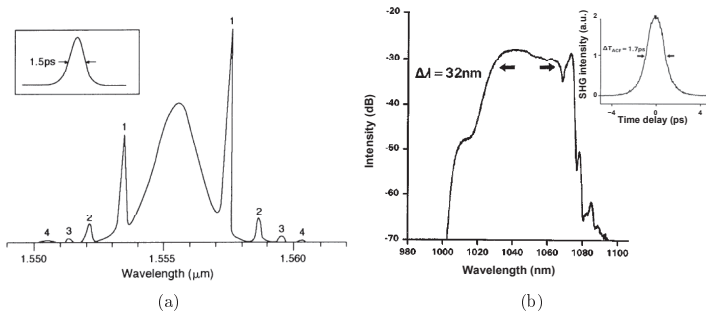

Figure 4.5: (a) Sech spectrum with sidebands, typical for soliton lasers. Mode-locking in this case was done by NPR. Inset shows the autocorrelation trace of the output pulses, close to the transform-limit. [43] (b) An Yb stretched-pulse laser (DM soliton) spectrum, and AC trace of the chirped output pulse in the inset. Note for the semi-log scale of the spectrum [46]

DM soliton regime Pulse formation and pulse evolution become more complex when the cavity is constructed with segments of large positive and negative dispersion fibers (/components). Such lasers have breathing solutions, i.e., the pulse duration varies, possibly an order of magnitude during one round-trip in the cavity. This efficiently reduces nonlinearity compared to soliton lasers and helps to avoid saturation of the mode-locking mechanism (saturable absorber) [44]. This regime is known as *stretched-pulse mode-locking* and the pulses as *dispersion-managed* (DM) *solitons*. It is shown that stable pulses can be formed with this technique when the net-cavity dispersion is close to zero, with net anomalous as well as net normal GVD [45].

A typical spectrum and AC function can be seen in Fig. 4.5 (b). The temporal pulse evolution in the cavity is shown in Fig. 1.8 in Section 1.4, in comparison with a similariton laser. The pulse energy in stretched-pulse lasers can be an order of magnitude higher than in a soliton lasers.

Wave-breaking free regime During pulse formation in the normal dispersion regime, SPM and normal GVD chirps the pulse. Excessive nonlinear phase shift

accumulated by the pulse as it traverses the cavity generally leads to optical wave-breaking, limiting the pulse energy, unless the pulses are reshaped resulting in a self-consistent propagation. In the reshaping mechanism (self-)amplitude modulation (e.g. by a saturable absorber) plays an important role.[10] Self-amplitude modulation can be realized by a nonlinear filter, that shapes the spectral or temporal profile of the pulse. For instance, gain dispersion [11] shapes the temporal profile of the chirped pulses by cutting off the wings of the spectrum. The resulting pulses are highly-chirped, and can be produced without dispersion compensation. It has to be noted, that more generally, amplitude modulation can be realized by a linear spectral filter, that acts in a similar way on chirped pulses as gain dispersion. With the access of the *wave-breaking free mode-locking* regime, output energies in access of 1 nJ were obtained. Notable subregimes are the self-similar laser and the so-called chirped pulse oscillator (CPO), described below. For further energy scaling, large-mode area fibers can be used. The highest pulse energy of 265 nJ generated directly by a femtosecond fiber laser was produced by using a large-mode area photonic crystal fiber [47].

Self-similar regime Pulse propagation in high-gain optical fiber amplifiers with normal dispersion has been studied by self-similarity analysis of the Nonlinear Schrö-dinger equation with gain. For an amplifier with a constant distributed gain, an exact asymptotic solution has been found that corresponds to a linearly chirped parabolic pulse that propagates self-similarly in the amplifier, subject to simple scaling rules [48]. The extension of this scheme to fiber lasers leads to a new regime of operation of mode-locked fiber lasers, known as *self-similar* or *similariton* regime. A typical spectrum can be seen in Fig. 4.6 (a) showing the parabolic shape on a semi-logarithmic scale. The pulses are always positively chirped inside the laser, with the temporal duration varying from ~ 3 to ~ 50 times the transform limit, and they can be dechirped outside the laser close to the transform-limit due to the linear chirp. Strong temporal breathing arises from the dispersion map and nonlinear pulse evolution (see Fig. 1.8 in Section 1.4 for the temporal pulse evolution in the cavity in comparison with a stretched-pulse laser). So far, pulse energies as high as 14 nJ have been generated by an Yb similariton fiber laser [49].

---

[10] The importance of the absorber is in contrast with the stretched-pulse regime, where self-amplitude modulation of the mode-locking mechanism is only needed for the initialization and stabilization of the inherently stable pulses.

[11] The finite gain bandwidth is usually taken into account as parabolic frequency dependence of gain.

Chirped pulse oscillator   *Chirped pulse oscillators* (CPOs) are originally used to refer to bulk solid-state lasers, such as Ti:sapphire. The feature that all CPOs have in common is the weak temporal breathing due to the weak dispersion map, which contrasts with the fiber lasers with clear pulse evolution [50]. In fiber lasers this scheme is applied by providing additional positive dispersion with negligible nonlinearity [51].

The resulting pulses generated by a CPO are highly chirped and have typically a spectrum with steep edges and flat top, as seen in Fig. 4.6 (b).

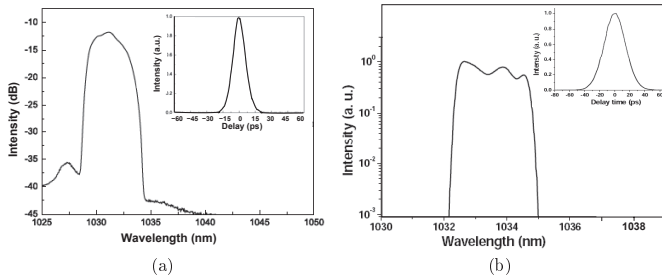(a)   (b)

Figure 4.6: (a) Measured parabolic spectrum of a similariton on a semi-logarithmic scale with the AC function in the inset [52], and (b) the corresponding results measured on a CPO output [51]

All-normal dispersion regime   Regarding the so-called *all-normal dispersion regime* (ANDi) as a single operating region, distinct from the self-similar and CPO regimes, and embedded in the wave-breaking free regime is controversial. Pulse shaping in ANDi lasers is based − besides positive GVD and SPM − on spectral filtering serving as self-amplitude modulation, by cutting off the temporal wings of the highly chirped pulses.[12]

Recently, a systematic investigation of a fiber laser utilizing a spectral filter was done by changing several parameters of the system. These parameters were the spectral bandwidth ($\Delta\Omega$), net-cavity dispersion (GDD_{net}) and the nonlinear phase shift (Φ_{NL}). The schematic of the setup on which the investigations were carried out can be seen in Fig. 4.7 and a plot of spectra and AC traces measured at different nonlinear phase shifts, are shown in Fig. 4.8. By increasing Φ_{NL}, the spectral shape

---

[12]In this sense, the difference to other regions in the wave-breaking free regime lies in the usage of a spectral filter directly, and not in realizing a distinct pulse shaping mechanism.

gradually changes from a parabolic shape to a broad and modulated shape. However, investigations on the temporal evolution suggest that the pulse propagation in the case of parabolic spectrum is similar to the CPO, as it exhibits very low temporal breathing. On the other hand, in the case of the broader spectrum with fringes, the temporal breathing ratio is ~ 4 and the spectrum changes significantly as well. The temporal evolution in this case is qualitatively the same as that of the similariton laser. Furthermore, the same trends can be observed with reducing the net-cavity dispersion and reducing the spectral filter bandwidth, i.e., increasing the 'strength of spectral filtering', as with the increase of Φ_{NL}:

$$\Phi_{NL} \sim 1/\Delta\Omega \sim 1/\mathrm{GDD}_{\mathrm{net}} \tag{4.1}$$

This is in accordance with the following principles. Higher $\mathrm{GDD}_{\mathrm{net}}$ causes higher temporal stretching which reduces Φ_{NL} through lower peak intensities. On the other hand, a certain value of GVD causes less temporal stretching on pulses with a narrower bandwidth, thus increases Φ_{NL}.

Gain-guided-soliton regime Further mode-locking regimes are discovered / can be distinguished. For example, solitary pulses, with a sech^2 shape are demonstrated to be generated by a fiber laser operating entirely in the normal dispersion regime [53].

4.2.3 Mode-locking by nonlinear polarization rotation

Fiber lasers can be mode-locked by using nonlinear birefringence to induce intensity-dependent changes in the state of polarization when orthogonally polarized components of a single pulse propagate in the fiber. A polarizer placed between two polarization controllers (PCs) acts as the mode-locking element. The PC placed after the polarizer changes the polarization state from linear to elliptical.[13] The polarization state evolves nonlinearly during propagation because of the different SPM- and XPM-induced phase shifts imposed on the two orthogonally polarized components. The state of polarization is nonuniform across the pulse because of the intensity dependence of the nonlinear phase shift. The second PC is adjusted in a way, that the polarization is linear in the central part of the pulse. Consequently, the polarizer lets the central intense part of the pulse pass but filters the low-intensity pulse wings. The net result is that the pulse is slightly shortened after one round-trip inside the ring cavity, an effect identical to that produced by a fast saturable absorber (e.g. Kerr-effect mode-locking [54]).

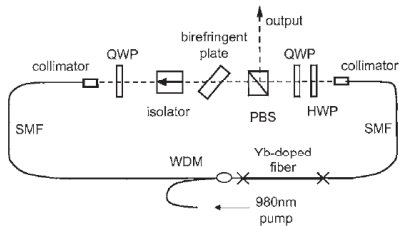[13]This might occur due to linear birefringence in the fiber as well.

Figure 4.7: Experimental setup of an ANDi laser; PBS: polarizing beam splitter, QWP: quarter-wave plate, SMF: single-mode fiber, WDM: wavelength division multiplexer, HWP: half-wave plate [39].
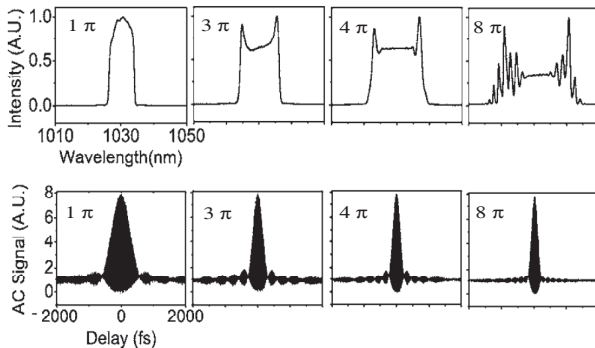

Figure 4.8: Output spectra with different nonlinear phase shifts $\Phi_{NL} \sim 1\pi, \sim 3\pi, \sim 4\pi, \sim 8\pi$, respectively. Bottom row: corresponding experimental dechirped interferometric AC functions [39].

4.2.4 Construction of mode-locked fiber lasers

Although a wide variety of fiber optic components are commercially available, they are not as reliable, and their parameters are not as easily controllable, as that of bulk elements. This fact raises difficulties in the development and control of all-fiber oscillators.

Fiber lasers around 1 µm are usually constructed with some kind of intra-cavity dispersion compensation to (at least partially) overcome the normal dispersion provided by silica fibers. Free space optics, such as gratings [49] and prisms [46], and lately photonic crystal fibers [55], higher-order mode fibers [56] or chirped fiber Bragg gratings [57] have been implemented as intra-cavity dispersion compensating

elements. However, for the ease of construction and use, and cost-effectiveness, it is desirable to design fiber oscillators without any dispersion compensation.

The pulse dynamics in dispersion-compensation free fiber lasers is dominated by the interplay between gain, self-phase modulation, dispersion and self-amplitude modulation acting as a filtering effect. Filtering with a 10 nm bandwidth spectral filter in an ANDi laser has lead to stable mode-locking of 3 nJ pulses dechirped to as short as 170 fs [41]. However, this setup employed free-space optics and such impressive results could not be reproduced by all-fiber configurations. Previous all-fiber oscillators produced picosecond pulses, owing to the strong spectral filtering [58], and in another approach ps pulses were generated by the pulse-shaping of the nonlinearity of a semiconductor saturable absorber mirror [59].

Lately, an all-fiber similariton fiber laser was reported, producing 0.8 nJ pulses, that were externally compressible to 627 fs, which is close to the transform-limit of the corresponding spectrum of 4.2 nm FWHM [52]. This laser had a unidirectional cavity, utilizing a fiber coupled saturable Bragg reflector in a bidirectional part via a polarizing beam splitter (PBS), hence we refer to it as a σ-shaped resonator. In our concept, we aimed to develop an all-fiber oscillator with the possibly simplest arrangement, and avoid multiple filtering − here, by the PBS −, that might lead to excessive narrowing of the output spectrum.

Very recently, an all-fiber normal dispersion ring laser was demonstrated [60]. It included a $\sim$ 15 nm bandwidth fiber filter, and a saturable absorber based on carbon nanotubes. The laser generated 1.5 ps, 3 nJ pulses that were compressible to 250 fs duration. However, the pedestals of the compressed pulses contained significant part of the energy because of the modulation of the spectrum.

Our purpose was to create an all-fiber, all-normal dispersion ring oscillator. The pulse-shaping in our arrangement is based on NPR and a polarizing element utilized for spectral and temporal filtering. Thus, the necessity for a fixed bandwidth spectral filter was eliminated as we aimed to avoid this element for the ease of design. It is also to be noted that the application of a fiber integrated bandwidth filter was not implemented until very recently [60]. The pulse characteristics were investigated at different positions in the oscillator in order to understand the pulse-shaping in more detail and also to find the optimal position of output for further applications.

4.3 Experimental setup

During our early experiments on mode-locked fiber lasers we have tried many con-figurations utilizing bulk optics which were changed to fiber integrated elements step-by-step. Some of these elements appeared only very recently and their perfor-mance is sometimes not reliable and/or could not be fully characterized. This refers to polarization changes for light propagating through the components, phase shifts and spectral transmittance. As we are not able to explain all of the results of the earlier experiments I will confine the description to the following setup.

The ring oscillator consists of the following fibers and fiber optic components, as shown in Fig. 4.9. A highly doped ytterbium fiber (YbF) is used as the gain media, backward pumped by a 980 nm laser diode via a 980/1030 nm wavelength-division multiplexer (WDM). To investigate the pulse characteristics right behind the gain fiber, a 90/10 splitter (OC_2) is placed between the WDM and the YbF. The WDM is followed by the semiconductor saturable absorber (SA) that is a commercially available absorber designed for use at around 1020 nm (Batop GmbH, SA-1020-40) and is responsible for the initiation and stabilization of mode-locking. A 10% output port (OC_3) is included after the SA. The single-mode fiber (SMF) pigtails between the YbF and the SA are $\sim$ 1.9 m, and the fiber section between the SA and the following PBS is $\sim$ 2 m. The length of these fiber sections is critical in the pulse-shaping mechanism that is based on the spectral broadening in the YbF and the nonlinear polarization evolution (NPE) in the SMF section [40]. The variation of the polarization state along the spectrum leads to a strong spectral filtering by the PBS. The PBS is followed by a splitter (OC_1) and an isolator (ISO) realizing the unidirectional cavity. Fiber polarization controllers (PC_1, PC_2) are applied on the fiber sections close to the PBS on both sides of it, but the mode-locked operation can be maintained when removing either of them. However, initiation of the mode-locking and adjustment of the desired mode of operation can be easily achieved by rotating the different paddles of the PCs.
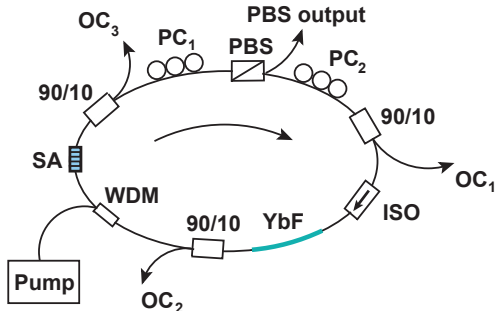
Figure 4.9: Experimental setup (PBS: polarizing beam splitter; PC: polarization controller; 90/10: 90/10 splitter; OC: output coupler; ISO: isolator; YbF: Yb-doped fiber; WDM: wavelength division multiplexer; SA: saturable absorber).

4.4 Experimental results

The above described oscillator produces stable mode-locking with low noise (according to the radio-frequency (RF) spectrum, shown in Fig. 4.10 (a)), and a repetition rate of 27.7 MHz. Besides the initiation of mode-locking the paddles of the PCs are responsible for various effects on the mode of operation. By adjusting the side $(\lambda/4)$ paddles the operation can be shifted from noise-like pulses [38] to noisy, Q-switched or cw mode-locking. These can be identified by observing the RF spectra and the autocorrelation functions, and some change on the optical spectrum can be observed as well. RF and optical spectra are shown in Fig. 4.3, Section 4.2.1, measured at a similar setup, with ~ 40 MHz repetition rate. The adjustment of PC_2 leads to wavelength tuning of more than 15 nm, as it can be seen in Fig. 4.10 (b). Furthermore the output coupling ratio of the PBS is most sensitive to the state of the third $(\lambda/4)$ paddle of PC_1. Under some circumstances the spectral width can be increased by increasing the output coupling ratio as well as by increasing the pump power.

The laser operates in the all-normal dispersion regime, where gain, self-phase modulation and dispersion is balanced by spectral (and temporal) filtering. As the output characteristics are extremely sensitive to the settings of the polarization controllers we might conclude that the nonlinear polarization rotation (NPR) together with the polarizer (PBS) has a crucial role in the filtering.

To observe the effect of the NPR we characterized the polarization state of the
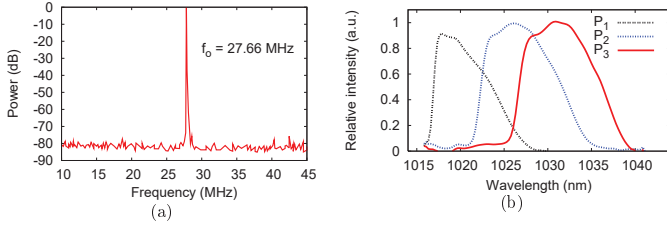
Figure 4.10: (a) The RF spectrum of the laser (f_o: central frequency). (b) Tunability, measured at OC_1.

laser along the spectrum at OC_3. This was carried out by measuring the spectra after a polarizer at the output as a function of the polarizer angle. Some of the measured spectra are shown in Fig. 4.11 (a) and the evaluated polarization states at different wavelengths are plotted in Fig. 4.12.[14] For stable pulse evolution spectral filtering is required which can be achieved using a PBS. When the polarization is set linear in the middle of the pulse, the PBS affects only the sides of the spectrum. Because of the linear chirping [15] this filtering leads to temporal pulse-shaping as well. The polarization at the lower wavelength edge of the spectrum is rather circular. This effect is observable at different states of the PCs as well. It is possibly connected to the saturation of the NPR at the tail of the pulse. The polarization at OC_1 is measured to be almost linear and constant along the spectrum.
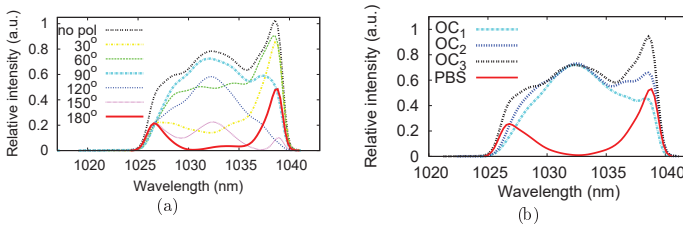
Figure 4.11: (a) Spectra measured at different polarizer angles at OC_3, and (b) spectra measured at the different output ports.

---

[14] The evaluation of the polarization state for a given spectral component is based on plotting the relative intensity values vs. polarization angles in polar coordinates.

[15] Linear chirping is demonstrated by our autocorrelation measurements after external compression of the pulses, described later in this section.

In order to investigate the laser dynamics the spectral and temporal characteristics of the pulses are measured. The spectra from OC_1 to OC_3 show asymmetric broadening with an increasing peak at the long wavelength edge, as plotted in Fig. 4.11 (b), possibly due to the higher gain at the leading edge of the propagating chirped pulse. The spectrum at OC_3 is split into the OC_1 and the PBS output spectra according to the polarization state (see the 180° and the 90° polarizer angle spectra in Fig. 4.11 (a) for comparison) resulting in a strong modulation of the PBS output spectrum.
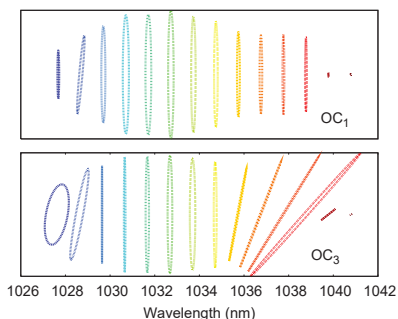

Figure 4.12: Polarization states at different wavelengths, measured at OC_1 and OC_3, respectively. Note that the relative phases of the evaluated polarization states measured at OC_3 compared to the polarization states measured at OC_1 are not appropriately aligned. The relative phase depends on the linear birefringence induced by bending of the fibers etc.

The temporal shape of the pulses is characterized by the autocorrelation functions. The width of the autocorrelation functions (ΔT_{AC}) measured at the laser outputs are 10-15 ps and have Gaussian shape except for the one at the PBS output (which looks like the sum of three Gaussians). The output pulses are compressed by a grating pair external to the resonator close to the Fourier-transform limit, implying a nearly linear chirp. The autocorrelation functions are shown in Fig. 4.13, plotted with red filled curves. The corresponding spectra are in the insets. Although there is some uncompensated positive third order dispersion, mainly the modulation in the spectra is responsible for the pedestals in the autocorrelation traces. This was verified by comparing the calculated autocorrelation functions of the transform-limited pulse with the chirped and externally compressed pulses, both corresponding to the measured spectra. The calculated autocorrelation functions of the compressed pulses (taking the second and third order dispersion of the cavity and the grating

pair into account) are plotted with black lines and the amplitude of the pedestals is similar in the case of transform-limited pulses as well. The pulse widths (ΔT_{pulse}) are estimated from the calculation of the compressed pulses. The shortest pulses are measured at the PBS output, however the quality is poor due to the spectral modulation. It can be seen, that from OC_1 towards the PBS output the spectral width increases and the compressed pulses get narrower as it is expected. Pulses with the highest quality i.e. lowest ratio of power in the pedestals are measured at OC_1.
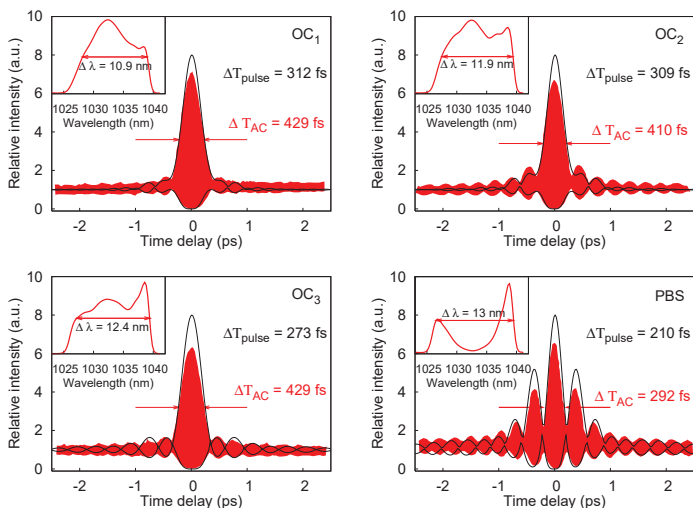

Figure 4.13: Measured (red filled curves) and fitted (black lines) autocorrelation functions at the OC_1, OC_2, OC_3, and PBS outputs after external compression by a grating pair. ΔT_{AC} is the width of the measured autocorrelation trace, ΔT_{pulse} is the estimated pulse width according to the calculations. Insets show the corresponding spectra and spectral widths.

In order to obtain a more practical laser the resonator was modified by removing the output couplers ($OC_{1,2,3}$) and the PBS was used as a single output port (see Fig. 4.14 (a)). In this case ~ 0.2 nJ pulses were measured at the output at $\sim$450 mW pumping power. The pulses were compressible to ~ 195 fs, with a lower ratio of the energy being in the pedestals as it can be observed in Fig. 4.14 (b). The laser had similar characteristics to the above investigated one. The difference is due to the

lower resonator loss resulting in lower threshold for cw mode-locking and due to a shorter resonator length (f_o = 42.6 MHz) with weaker NPR. The latter results in a lower contrast in the modulation of the spectrum measured at the PBS leading to higher pulse quality. It is to mention, that the repetition rate can be further increased with this setup.

For most applications amplification of the laser output is necessary. To achieve high pulse quality amplification of a source with unmodulated spectrum would be ideal with further compression. For this reason OC_1 should be maintained as the main output with high pulse quality, unmodulated (parabolic-like) spectrum and linear polarization. Higher pulse energy can be obtained by increasing the output coupling ratio. The PBS output can be used for monitoring.
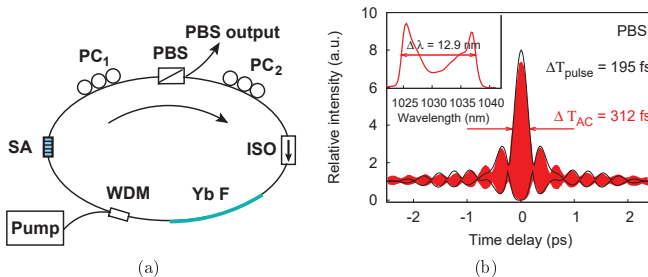

Figure 4.14: (a) Experimental setup of a modified oscillator with a single output (PBS rejection port) and (b) measured (red filled curves) and fitted (black lines) autocorrelation functions with the spectrum in the inset.

4.5   Conclusion

We have demonstrated an all-fiber Yb ring oscillator without any intra-cavity dispersion compensation. Four output ports have been characterized and compared. The broadest spectrum was measured at the PBS rejection port but it was strongly modulated. Other spectra at the 90/10 splitter outputs had more parabolic-like shape. The autocorrelation widths at all outputs are $\sim 10 - 15$ ps and the pulses can be compressed close to the Fourier-transform limit by a grating pair. The shortest compressed pulses are 210 fs, and the RF spectrum as well as the pulse train observed on an oscilloscope showed stable cw mode-locking with a high S/N ratio. Furthermore, a shorter oscillator was presented to show similar characteristics. The

oscillator with a single PBS rejection port generated pulses compressible to as short as 195 fs with a relatively high pulse quality.

Summary

Waveguidance of light by optical fibers can be described by the Helmholtz equation. With several considerations and assumptions that hold for ultrashort pulses in optical fibers, two important equations can be deduced, one of which determines the transversal mode distribution, the other one determines longitudinal propagation of pulses. By the simulations of fiber modes, the design of optical fibers can be supported. The other equation derived from the Helmholtz equation, is the Nonlinear Schrödinger equation, which determines the spectral and temporal evolution of pulses propagating along the fiber. The most important phenomena in the context of pulse propagation are dispersion and nonlinearities. Photonic crystal fibers (PCFs) offer a wide range of design parameters, which enable precise control of the nonlinear coefficient and the dispersion profile. This feature gives rise to numerous applications, such as dispersion control and distortion-free delivery of ultrashort pulses by the elimination of nonlinearity in PCFs. On the other hand, it may also provide advantages for nonlinear phenomena by the application of small-core area PCFs.

During my Ph.D. work, I was dealing with the generation of ultrashort pulses in fiber lasers, the propagation of such pulses in photonic crystal fibers and the design of special purpose photonic crystal fibers. Parts of these topics included theoretical work with numerical simulations. However, most of the results described in the theses are experimental, and the research was essentially motivated by practical applications. The theses are itemized as follows.

Thesis 1 We have proposed a method for the proper design of photonic bandgap dielectric structures used at grazing incidence [T1]. The theory is based on the one-dimensional multilayer design, that I applied to one- and two-dimensional structures. I have compared plane photonic bandgap dielectric mirrors of different design principles and suggested plane dielectric mirrors to be used in grazing incidence as laser mirrors. Based on one-dimensional results, we extended the model to two-dimensional photonic bandgap dielectric structures and applied to all-silica hollow-core Bragg photonic bandgap fibers. I investigated the principles of the elimination of leaking modes in realistic hollow-core Bragg photonic bandgap fibers. I found leaking mode free structures and we compared the results to simulations done by the full-vectorial finite element method, taking the appropriate fiber structure into account. Results show that the one-dimensional model is capable of giving estimates for the design of leaking mode free hollow-core Bragg photonic bandgap fibers and

thus represents an effective complementary tool to simulations done by complicated and time-consuming full-wave solvers.

Thesis 2   Pulse compression below the Fourier transform limit can be realized by nonlinear spectral broadening. For sub-nanojoule pulse energies, this is achieved in a photonic crystal fiber with reduced core size. According to simulations of pulse propagation and optimization of the pre-chirp and subsequent dispersion-compensation coefficients, I have experimentally demonstrated two-fold pulse compression on nearly transform limited 24 fs pulses from a Ti:sapphire laser around 800 nm [T2].

Thesis 3   We have developed a passively mode-locked, all-fiber, all-normal dispersion ytterbium ring oscillator, working at 1.03 µm. The laser produces picosecond pulses, that can be dechirped by an external grating pair to ~ 200 fs pulse durations [T3]. The pulse-shaping in the oscillator is based on nonlinear polarization evolution in the fiber sections together with spectral and temporal filtering by a polarizing element. We have investigated the laser characteristics as an aim to better understand the theory of mode-locking in fiber oscillators, operating in the normal dispersion regime.

Publications and references

4.6   PhD related publications

Refereed papers

[T1]   J. Fekete, Z. Várallyay, R. Szipőcs, "Design of high bandwidth one- and two-dimensional photonic bandgap dielectric structures at grazing incidence of light," Applied Optics **47**, 5330-5336 (2008).

[T2]   Z. Várallyay, J. Fekete, Á. Bányász, R. Szipőcs, "Optimizing input and output chirps up to the third-order for sub-nanojoule, ultra-short pulse compression in small core area PCF," Applied Physics B **86**, 567-572 (2007).

[T3]   J. Fekete, A. Cserteg, R. Szipőcs, "All-fiber, all-normal dispersion ytterbium ring oscillator," Laser Physics Letters **6**, 49-53 (2009).

Other PhD related publications

[T1.1] J. Fekete, Z. Várallyay, R. Szipőcs, "Design of leaking mode free hollow-core photonic bandgap fibers," in *Optical Fiber Communication Conference*, OSA Technical Digest Series (Optical Society of America, 2008), paper JWA4.

[T2.1] Z. Várallyay, J. Fekete, Á. Bányász, R. Szipőcs, "Sub-nanojoule pulse compression in small core area photonic crystal fibers below the zero dispersion wavelength," *Trends in Optics and Photonics* **98**, 571-576 (2005).

[T2.2] Z. Várallyay, J. Fekete, Á. Bányász, S. Lakó, R. Szipőcs, "Sub-nanojoule pulse compression down to 6 fs in photonic crystal fibers," in *Conference on Lasers and Electro-Optics*, CLEO Europe, Munich, Germany, June, 2005.

[T2.3] R. Szipőcs, J. Fekete, Á. Bányász, Z. Várallyay, "Pulse Compression with Highly Nonlinear Photonic Crystal Fibers by Optimization of Input and Output Chirp Parameters up to the Third-Order," in *Optical Amplifiers and Their Applications*, Technical Digest (CD) (Optical Society of America, 2005), paper ME6.

[T2.4] Z. Várallyay, J. Fekete, Á. Bányász, S. Lakó, R. Szipőcs, "Sub-nanojoule pulse compression down to 6 fs in photonic crystal fibers," in *Conference on Lasers and Electro-Optics,* CLEO/QELS Conference, Baltimore, Maryland, USA, May 22-27, 2005, paper JThE21.

[T2.5] Z. Várallyay, J. Fekete, Á. Bányász, S. Lakó, R. Szipőcs, "Sub-nanojoule pulse compression down to 6 fs in photonic crystal fibers," in *Advanced Solid State Photonics Conference*, Vienna, Austria, February 6-9, 2005, paper WD2.

[T3.1] Fekete J., Cserteg A., Szipőcs R., "Módusszinkronizált, normál diszperziójú szálintegrált itterbium ring oszcillátor," *Kvantumelektronika konferencia*, Budapest, 2008.

4.7   Other publications

Refereed papers

[J1] Z. Várallyay, K. Saitoh, J. Fekete, K. Kakihara, M. Koshiba, R. Szipőcs, "Reversed dispersion slope photonic bandgap fibers for broadband dispersion control in femtosecond fiber lasers," Opt. Express **16**, 15603-15616 (2008).

[J2] B. Rózsa, G. Katona, E. S. Vizi, Z. Várallyay, A. Sághy, L. Valenta, P. Maák, J. Fekete, Á. Bányász, R. Szipőcs, "Random access three-dimensional two-photon microscopy," Applied Optics **46**, 1860-1865 (2007).

[J3] P. Dombi, P. Antal, J. Fekete, R. Szipőcs, Z. Várallyay, "Chirped-pulse supercontinuum generation with a long-cavity Ti:sapphire oscillator," Applied Physics B **88**, 379-384 (2007).

Other journal papers

[J4] B. Rozsa, E. S. Vizi, G. Katona, A. Lukács, Z. Várallyay, A. Sághy, L. Valenta, P. Maák, J. Fekete, Á. Bányász, R. Szipőcs, "Real time 3D nonlinear microscopy," *Trends in Optics and Photonics* **98**, 858-863 (2005).

[J5] Szipőcs R., Fekete J., Katona G., Rózsa B., "Nemlineáris mikroszkópia és biológiai-orvosi alkalmazásai," *A kvantumoptika és -elektronika legújabb eredményei*, ELFT Atom-, Molekulafizikai és Kvantumelektronikai Szakcsoport Tavaszi Iskola 2005.

Patents

[P1] Vizi E. Szilveszter, Szipőcs Róbert, Rózsa Balázs, Maák Pál, Fekete Júlia, Valenta László, Katona Gergely, Kalló Péter, Osvay Károly, "Valós idejű, 3D, nemlineáris mikroszkóp mérőrendszer, valamint eljárás annak alkalmazására," P0500143 (2005.01.27.)

[P2]   E. S. Vizi, R. Szipőcs, B. Rózsa, P. Maák, J. Fekete, L. Valenta, G. Katona,
        P. Kalló, K. Osvay, "Real-time, 3D, non-linear microscope measuring system
        and method for application of the same," European patent, PCT Appl. No. 06
        710 202.0-2217

[P3]   E. S. Vizi, R. Szipőcs, B. Rózsa, P. Maák, J. Fekete, L. Valenta, G. Katona,
        P. Kalló, K. Osvay, "Real-time, 3D, non-linear microscope measuring system
        and method for application of the same," US Pat. Appl. No. 11/814.917,
        09/26/2007

Conferences

[C1]   Z. Várallyay, J. Fekete, R. Szipőcs, "Higher order mode photonic bandgap
        fibers for dispersion control," in *Conference on Lasers and Electro-Optics*,
        CLEO/QELS Conference, OSA Technical Digest Series (Optical Society of
        America, 2008), paper JThA48.

[C2]   Z. Várallyay, J. Fekete, R. Szipőcs, "Higher-order mode photonic bandgap
        fibers with reversed dispersion slope," in *Optical Fiber Communication Con-
        ference*, OSA Technical Digest Series (Optical Society of America, 2008), pa-
        per JWA8.

[C3]   P. Dombi, P. Antal, R. Szipőcs, Z. Várallyay, J. Fekete, "Chirped-pulse su-
        percontinuum generation with a 200-nJ Ti:sapphire oscillator," in *Conference
        on Lasers and Electro-Optics*, CLEO Europe-IQEC 2007, 17-22 June 2007,
        Munich, Germany, paper CF-19-MON.

[C4]   P. Dombi, P. Antal, R. Szipőcs, Z. Várallyay, J. Fekete, "Optimizing and
        pulse compression of a 200-nJ chirped pulse Ti:sapphire oscillator," in *8th In-
        ternational Symposium on Laser Precision Microfabrication* 2007, 24-28 April
        2007, University of Vienna, Vienna, Austria, paper P-11.

[C5]   B. Rozsa, G. Katona, E. S. Vizi, A. Lukács, Z. Várallyay, A. Sághy, L. Va-
        lenta, P. Maák, J. Fekete, Á. Bányász, R. Szipőcs, "Real time 3D two-photon
        microscopy for neurology," in *Biomedical Optics Conference*, March 19-22,
        2006, Fort Lauderdale, Florida, Technical Digest (CD) (Optical Society of
        America, 2006), paper TuI67.

[C6]   J. Fekete, Á. Bányász, R. Szipőcs, G. Katona, A. Lukács, B. Császár, Z.
        Várallyay, A. Sághy, P. Maák, B. Rózsa, E. S. Vizi, "Real time 3D nonlin-

ear microscopy," in *Conference on Lasers and Electro-Optics*, CLEO Europe, Munich, Germany, June , 2005.

[C7]   J. Fekete, Á. Bányász, R. Szipőcs, G. Katona, A. Lukács, B. Császár, Z. Várallyay, A. Sághy, P. Maák, B. Rózsa, E. S. Vizi, "Real time 3-D nonlinear microscopy," in *Conference on Lasers and Electro-Optics,* CLEO/QELS Conference, Baltimore, Maryland, USA, May 22-27, 2005, paper JThE36.

[C8]   J. Fekete, Á. Bányász, R. Szipőcs, G. Katona, A. Lukács, B. Császár, Z. Várallyay, A. Sághy, P. Maák, B. Rózsa, E. S. Vizi, "Real time 3D nonlinear microscopy," in *Advanced Solid State Photonics Conference*, Vienna, Austria, February 6-9, 2005, paper WB21.

[C9]   R. Szipőcs, Á. Bányász, J. Fekete , Z. Várallyay, A. Lukács, "Chirped pulse fiber delivery system for high speed, high spatial resolution 3D two-photon microscopy," in *Conference of ESF Femtochemistry and Femtobiology (ULTRA) program*, Pécs, Hungary, March 25-28, 2004.

[C10] R. Szipőcs, J. Hebling, Á. Bányász, J. Fekete, A. Lukács, "Advances in fs laser sources utilizing chirped mirror technology," in *Conference of ESF Femtochemistry and Femtobiology (ULTRA) program*, Pécs, Hungary, March 25-28, 2004.

[C11] B. Rózsa, G. Katona, B. Lendvai, E.S. Vizi, P. Maák, Z. Várallyay, L. Valenta, T. Volosin, A. Vági, Á. Bányász, A. Lukács, J. Fekete, R. Szipőcs, "Fast scanning and uncaging strategies in 3D two-photon microscopy," in *IBRO International Workshop on Neuronal Circuits: from Elementary to Complex Functions*, 2004.

[C12] B. Rózsa, Sz. E. Vizi, Á. Bányász, J. Fekete, R. Szipőcs, "Véletlen címzésű, sokcsatornás, 3D kétfoton abszorpciós fluoreszcencia mikroszkóp optikai leképező rendszerének felbontás mérése fluoreszcens gömbökkel," *Kvantumelektronika konferencia*, Budapest, 2003.

4.8 References

[1] G.P. Agrawal, "*Nonlinear Fiber Optics*," Academic Press, San Diego (1995) ISBN: 0-12-045143-3.

[2] http://en.wikipedia.org/wiki/Physics

[3] M. Szpulak, W. Urbanczyk, E. Serebryannikov, A. Zheltikov, A. Hochman, Y. Leviatan, R. Kotynski, K. Panajotov, "Comparison of different methods for rigorous modeling of photonic crystal fibers," Opt. Express **14,** 5699-5714 (2006).

[4] P. Yeh, A. Yariv, E. Marom, "Theory of Bragg fiber," J. Opt. Soc. Am. **68,** 1196-1201 (1978).

[5] W.H. Reeves, D.V. Skryabin, F. Biancalana, J.C. Knight, P.St.J. Russell, F.G. Omenetto, A. Efimov, A.J. Taylor, "Transformation and control of ultrashort pulses in dispersion-engineered photonic crystal fibres," Nature **424,** 511-515 (2003).

[6] J. Broeng, T. Søndergaard, S.E. Barkou, P.M. Barbeito, A. Bjarklev, "Wave-guidance by the photonic bandgap effect in optical fibres," J. Opt. A: Pure Appl. Opt. **1**, 477-482 (1999).

[7] T. Schreiber, B. Ortaç, J. Limpert, A. Tünnermann, "On the study of pulse evolution in ultra-short pulse mode-locked fiber lasers by numerical simulations," Opt. Express **15**, 8252-8262 (2007).

[8] J.C. Diels, W. Rudolph, "*Ultrashort laser pulse phenomena: Fundamentals, Techniques, and Applications on a Femtosecond Time Scale,*" (Optics and Photonics Series) Academic Press, San Diego (1996) ISBN: 0-12-215492-4.

[9] R.F. Cregan, B.J. Mangan, J.C. Knight, T.A. Birks, P.St.J. Russell, P.J. Roberts, D.C. Allan, "Single-Mode Photonic Band Gap Guidance of Light in Air," Science **285** 1537-1539 (1999).

[10] H.A. Haus, "Mode-locking of lasers," IEEE J. Sel. Top. Quantum Electron. **6,** 1173-1185 (2000).

[11] H.A. Macleod, "*Thin-film optical filters,*" 2nd edition, Adam Hilger Ltd., Bristol, GB, (1986) ISBN: 0-85274-784-5.

[12] F. Mezei, "Novel polarized neutron devices: supermirror and spin component amplifier," Commun. Phys. **1,** 81-85 (1976).

[13] E.J. Mayer, J. Möbius, A. Euteneuer, W.W. Rühle, R. Szipőcs, "Ultrabroad-band chirped mirrors for femtosecond lasers," Opt. Letters **22,** 528-530 (1997).

[14] I.D. Jung, F.X. Kärtner, N. Matuschek, D.H. Sutter, F. Morier-Genoud, G. Zhang, U. Keller, V. Scheuer, M. Tilsch, T. Tschudi, "Self-starting 6.5 fs pulses from a Ti:sapphire laser," Opt. Letters **22,** 1009-1011 (1997).

[15] K. Ferencz, R. Szipőcs, "Recent development of laser optical coatings in Hungary," Opt. Eng. **32,** 2525-2538 (1993).

[16] A. Stingl, Ch. Spielmann, F. Krausz, R. Szipőcs, "Generation of 11-fs pulses from a Ti:sapphire laser without the use of prisms," Opt. Letters **19,** 204-206 (1994).

[17] J. Hebling, E.J. Mayer, J. Kuhl, R. Szipőcs, "Chirped-mirror dispersion-compensated optical parametric oscillator," Opt. Letters **20,** 919-921 (1995).

[18] Zs. Bor, B. Rácz, G. Szabó, Z.Gy. Horváth, "Two-dimensional halo laser performance," Phys. Letters **80A,** 153-155, (1980).

[19] P.St.J. Russell, "Photonic Crystal Fibers," IEEE J. Lightwave Technol. **24,** 4729-4749 (2006).

[20] G. Bouwmans, F. Luan, J. Knight, P.St.J. Russell, L. Farr, B. Mangan, H. Sabert, "Properties of a hollow-core photonic bandgap fiber at 850 nm wavelength," Opt. Express **11,** 1613-1620 (2003).

[21] G. Vienne, Y. Xu, C. Jakobsen, H.J. Deyerl, J. Jensen, T. Sorensen, T. Hansen, Y. Huang, M. Terrel, R. Lee, N. Mortensen, J. Broeng, H. Simonsen, A. Bjarklev, A. Yariv, "Ultra-large bandwidth hollow-core guiding in all-silica Bragg fibers with nano-supports," Opt. Express **12,** 3500-3508 (2004).

[22] M. Foroni, D. Passaro, F. Poli, A. Cucinotta, S. Selleri, J. Laegsgaard, A. Bjarklev, "Confinement loss spectral behavior in hollow-core Bragg fibers," Opt. Lett. **32,** 3164-3166 (2007).

[23] K. Saitoh, N. Mortensen, M. Koshiba, "Air-core photonic band-gap fibers: the impact of surface modes," Opt. Express **12,** 394-400 (2004).

[24] C.M. Smith, N. Venkataraman, M.T. Gallagher, D. Müller, J.A. West, N.F. Borrelli, D.C. Allan, K.W. Koch, "Low-loss hollow-core silica/air photonic bandgap fibre," Nature **424**, 657-659 (2003).

[25] http://mintaka.sdsu.edu/GF/explain/optics/refr.html

[26] Z. Várallyay, J. Fekete, R. Szipőcs, "Higher-Order Mode Photonic Bandgap Fibers with Reversed Dispersion Slope," in *Optical Fiber Communication Conference*, OSA Technical Digest Series (Optical Society of America, 2008), paper **JWA8**.

[27] A. Baltuška, Z. Wei, M.S. Pshenichnikov, D.A. Wiersma, R. Szipőcs, "All-solid-state cavity-dumped sub-5-fs laser," Applied Physics B **65,** 175-188 (1997).

[28] M. Nisoli, S. De Silvestri, O. Svelto, R. Szipőcs, K. Ferencz, C. Spielmann, S. Sartania, F. Krausz, "Compression of high-energy laser pulses below 5 fs," Opt. Letters **22,** 522-524 (1997).

[29] S. Lakó, J. Seres, P. Apai, J. Balázs, R.S. Windeler, R. Szipőcs, "Pulse compression of nanojoule pulses in the visible using microstructure optical fiber and dispersion compensation," Applied Physics B **76,** 267-275 (2003).

[30] G. McConnell, E. Riis, "Ultra-short pulse compression using photonic crystal fibre," Applied Physics B **78,** 557-563 (2004).

[31] B. Schenkel, R. Paschotta, U. Keller, "Pulse compression with supercontinuum generation in microstructure fibers," J. Opt. Soc. Am. B **22,** 687-693 (2005).

[32] B. Császár, A. Kőházi-Kis, R. Szipőcs, "Low reflection loss ion-beam sputtered negative dispersion mirrors with MCGTI structure for low pump threshold compact femtosecond pulses lasers," in *Advanced Solid State Photonics Conference*, 2005 Technical Digest on CD-ROM (The Optical Society of America, Washington, DC, 2005), paper **WB17,** ISBN: 1-55752-781-4

[33] http://www.crystal-fibre.com

[34] http://www.fslasers.com

[35] F.Ö. Ilday, J. Buckley, L. Kuznetsova, F.W. Wise, "Generation of 36-femtosecond pulses from a ytterbium fiber laser," Opt. Express **11,** 3550-3554 (2003).

[36] C.K. Nielsen, "Mode Locked Fiber Lasers: Theoretical and Experimental Developments," PhD theses, University of Aarhus, Denmark (2006).

[37] G.P. Agrawal, "*Applications of nonlinear fiber optics*,' Academic Press, San Diego (2001) ISBN: 0-12-045144-1.

[38] M. Horowitz, Y. Barad, Y. Silberberg, "Noiselike pulses with a broadband spectrum generated from an erbium-doped fiber laser," Opt. Letters **22,** 799-801 (1997).

[39] A. Chong, W.H. Renninger, F.W. Wise, "Properties of normal-dispersion femtosecond fiber lasers," J. Opt. Soc. Am. B **25**, 140-148 (2008).

[40] A. Ruehl, D. Wandt, U. Morgner, D. Kracht, "On wave-breaking free fiber lasers mode-locked with two saturable absorber mechanisms," Opt. Express , **16,** 8181-8189 (2008).

[41] A. Chong, J. Buckley, W. Renninger, F. Wise, "All-normal-dispersion femtosecond fiber laser," Opt. Express **14,** 10095-10100 (2006).

[42] D.U. Noske, N. Pandit, J.R. Taylor, "Source of spectral and temporal instability in soliton fiber lasers," Opt. Letters **17,** 1515-1517 (1992).

[43] D.U. Noske, N. Pandit, J.R. Taylor, "Source of spectral and temporal instability in soliton fiber lasers," Opt. Letters **17**, 1515- (1992); Electron. Letters **28**, 2185 (1992).

[44] K. Tamura, J. Jacobson, H.A. Haus, E.P. Ippen, J.G. Fujimoto, "77-fs pulse generation from a stretched-pulse mode-locked all-fiber ring laser," Opt. Letters **18**, 1080-1082 (1993).

[45] H.A. Haus, K. Tamura, L.E. Nelson, E.P. Ippen, "Stretched-pulse additive pulse mode-locking in fiber ring lasers: Theory and experiment," IEEE J. Quantum Electron. **31**, 591-598 (1995).

[46] V. Cautaerts, D.J. Richardson, R. Paschotta, D.C. Hanna, "Stretched pulse Yb^{3+}:silica fiber laser," Opt. Letters **22,** 316-318 (1997).

[47] B. Ortaç, O. Schmidt, T. Schreiber, J. Limpert, A. Tünnermann, A. Hideur, "High-energy femtosecond Yb-doped dispersion compensation free fiber laser," Opt. Express **15,** 10725-10732 (2007).

[48] V.I. Kruglov, A.C. Peacock, J.D. Harvey, J.M. Dudley, "Self-similar propagation of parabolic pulses in normal-dispersion fiber amplifiers," J. Opt. Soc. Am. B **19** 461-469 (2002).

[49] J.R. Buckley, F.W. Wise, F. Ö. Ilday, T. Sosnowski, "Femtosecond fiber lasers with pulse energies above 10 nJ," Opt. Letters **30,** 1888-1890 (2005).

[50] M. Siegel, G. Palmer, M. Emons, M. Schultze1, A. Ruehl, U. Morgner, "Pulsing dynamics in Ytterbium based chirped-pulse oscillators," Opt. Express **16**, 14314-14320 (2008).

[51] B. Ortaç, M. Plötner, J. Limpert, A. Tünnermann, "Self-starting passively mode-locked chirped-pulse fiber laser," Opt. Express **15,** 16794-16799 (2007).

[52] O. Prochnow, A. Ruehl, M. Schultz, D. Wandt, D. Kracht, "All-fiber similariton laser at 1 µm without dispersion compensation," Opt. Express **15,** 6889-6893 (2007).

[53] J.W. Lou, M. Currie, F.K. Fatemi, "Experimental measurements of solitary pulse characteristics from an all-normal-dispersion Yb-doped fiber laser," Opt. Express **15**, 4960-4965 (2007).

[54] K. Sala, M. Richardson, N. Isenor, "Passive mode locking of lasers with the optical Kerr effect modulator," IEEE J. Quantum Electron. **13**, 915-924 (1977).

[55] A. Ruehl, O. Prochnow, M. Engelbrecht, D. Wandt, D. Kracht, "Similariton fiber laser with a hollow-core photonic bandgap fiber for dispersion control," Opt. Letters **32,** 1084-1086 (2007).

[56] J.W. Nicholson, S. Ramachandran, S. Ghalmi, "A passively-modelocked, Yb-doped, figure-eight, fiber laser utilizing anomalous-dispersion higher-order-mode fiber," Opt. Express **15,** 6623-6628 (2007).

[57] O. Katz, Y. Sintov, Y. Nafcha, Y. Glick, "Passively mode-locked ytterbium fiber laser utilizing chirped-fiber-Bragg-gratings for dispersion control," Opt. Commun. **269,** 156-165 (2007).

[58] C.K. Nielsen, S.R. Keiding, "All-fiber mode-locked fiber laser," Opt. Letters **32,** 1474-1476 (2007).

[59] R. Herda, O.G. Okhotnikov, "Dispersion compensation-free fiber laser mode-locked and stabilized by high-contrast saturable absorber mirror," IEEE J. Quantum Electron. **40,** 893-899 (2004).

[60] K. Kieu, F.W. Wise, "All-fiber normal-dispersion femtosecond laser," Opt. Express **16,** 11453-11458 (2008).

Acknowledgements

Abbreviations and notations

1D	one dimensional
2D	two dimensional
AC	autocorrelation
ANDi	all-normal dispersion
β	propagation constant
CPO	chirped pulse oscillator
c	speed of light in vacuum
cw	continous wave
GDD	group delay dispersion
GDD_net	net cavity GDD
GVD	group velocity dispersion
E	electric field envelope, see Eq. 1.3
$\mathbf{E}$	electric field vector
$\mathbb{E}$	pulse energy
ε_0	vacuum permittivity
FEM	finite element method
fs	femtosecond (10^{-15} s)
FWHM	full width at half maximum
Φ_NL	nonlinear phase shift
HC	hollow-core
ISO	isolator
$\Im$	imaginary part
k_0	wave number
χ	susceptibility
L	physical path length
LMA	large mode area
λ	wavelength
λ_0	central wavelength
ML	multilayer
μ_0	vacuum permeability
n	refractive index
n_eff	effective refractive index

n_H	refractive index of the high index layer
n_L	refractive index of the low index layer
NL	nonlinear
NPE	nonlinear polarization evolution
NPR	nonlinear polarization rotation
OC	output coupler
P	induced electric polarization
PBG	photonic bandgap
PBF	photonic bandgap fiber
PBS	polarizing beam splitter
PC	polarization controller
PCF	photonic crystal fiber
PT	physical thickness
r	radius
r	spatial coordinate
$\Re$	real part
RF	radio-frequency (spectrum)
SA	saturable absorber
SEM	scanning electron microscope
SFF	silica filling fraction
SMF	(step-index) single mode fiber
SPM	self-phase modulation
S/N	signal-to-noise (ratio)
t	time
TIR	total internal reflection
Ti:sapphire	titanium-sapphire
TMM	transfer matrix method
TOD	third order dispersion
Θ_0	angle of incidence
WDM	wavelength division multiplexer
XPM	cross-phase modulation
Yb	ytterbium
z	coordinate parallel to the fiber axis
ω	angular frequency
$\Delta\Omega$	spectral bandwidth

Conclusion

During my Ph.D. work, I was dealing with topics on the generation of ultrashort pulses in fiber lasers, the propagation of such pulses in photonic crystal fibers and the design of hollow-core photonic crystal fibers. Some part of the these topics included theoretical work, but as the research was essentially motivated by practical applications, most of the results described in the theses are experimental.

Ultrashort pulses are originally generated by dye or solid-state lasers. Due to the advances in optical fiber technology, considerable attention has been drawn by fiber lasers, for their compactness. In contrast to traditional passively mode-locked lasers, recently it was shown, that stable solutions can be found in the case of net normal cavity dispersion. Such systems eliminate the need for dispersion compensation in the cavity and enhance the possible output pulse energies. We developed an all-fiber ytterbium laser producing picosecond pulses, that are compressible to $\sim$200-400 fs external to the cavity [T3]. The laser operated in the "all-normal dispersion" regime, around 1.03 µm.

Compression of chirped pulses by dispersion-compensation is possible by the use of fiber integrated components. However, their use is often limited by the nonlinear interaction of the relatively high peak power of pulses with the silica core. A promising route to avoid nonlinearity is the application of hollow-core (Bragg) photonic crystal fibers, in which most of the energy of the pulse is confined in air. It was found, however, that the silica struts in realistic hollow-core fibers, holding the space between silica layers cause a loss mechanism, called leaking modes. Our investigations on one-dimensional grazing incidence dielectric multilayer structures showed, that the leaking modes can be eliminated by appropriate design of the structure. One-dimensional calculations were compared to the finite element method that simulated the appropriate fiber structure [T1]. The qualitative agreement between the simulation results showed that the one-dimensional model is capable of giving estimates for the bandgap, and thus it is a useful complementary tool in the design of such fibers.

Dispersion-compensation is not sufficient for compressing pulses below the Fourier transform limit. For this purpose, spectral broadening is necessary, which can be realized by nonlinear phenomena in optical fibers. For relatively low peak powers, the nonlinear spectral broadening can be achieved in photonic crystal fibers with reduced core size. According to our simulations of pulse propagation and optimization of dispersion-compensation coefficients, we experimentally demonstrated pulse compression on nearly transform-limited 24 fs pulses from a Ti:sapphire laser [T2].

Összefoglalás

Doktori munkám során ultrarövid impulzusok előállításával, fotonikus kristály szálban való terjedésével és légmagos fotonikus kristály szálak tervezésével foglalkoztam. Ezeknek a témáknak egy része elméleti munka, de mivel a kutatást gyakorlati alkalmazások motiválták, az eredmények nagyobb része kísérleti munkán alapul.

Ultrarövid impulzusokat hagyományosan szilárdtest lézerekkel állítanak elő. Az optikai szálak területén elért technológiai fejlődés hatására azonban egyre nagyobb az igény és lehetőség arra, hogy ezeket száloptikai lézerek váltsák fel. A hagyományos passzívan módusszinkronizált lézerekkel ellentétben kimutatták, hogy a rezonátor össz-diszperzióját tekintve a normál diszperziós tartományban is kialakulhat stabil impulzus vonulat. Ilyen rendszerekben elkerülhető a rezonátoron belüli diszperzió-kompenzálás, továbbá a lehetséges impulzus energia is nagyobb. Kifejlesztettünk egy teljesen szálintegrált itterbium lézert, amely pikoszekundumos impulzusokat generál [T3]. Ezek a rezonátoron kívül ∼200-400 fs-ra kompresszálhatók. A lézer az úgynevezett "teljesen normál diszperziós" tartományban működik, 1.03 µm hullámhosszon.

"Csörpölt" impulzusok diszperzió-kompenzálással való összenyomása megoldható száloptikai komponensekkel. Ezeknek a használatát azonban limitálja az impulzusok relatíve magas csúcsintenzitásának nemlineáris kölcsönhatása az üvegszál magjával. Egyik lehetőség a nemlinearitás elkerülésére a légmagos (Bragg) fotonikus kristály szálak használata, melyekben az impulzus energiájának nagy része a levegő magban koncentrálódik. Ilyen szálaknál problémát jelent az üvegrétegek közötti távtartó üvegrudacskák jelenléte, ugyanis ezek egy veszteségi mechanizmus, az úgynevezett "szivárgó módusok" okozói. Egy dimenziós súrlódó beesésre tervezett dielektrikum rétegszerkezeteken való vizsgálatainkkal kimutattuk, hogy a szivárgó módusok a szerkezet megfelelő megtervezésével megszűntethetők [T1]. Számításainkat összehasonlítottuk a véges-elem módszerrel, mely a tényleges szerkezetet vette figyelembe. A kvalitatív egyezés igazolta, hogy az egy dimenziós modell alkalmas a "bandgap" becslésére, és ezáltal a szerkezet megtervezésében hatékony segítséget nyújt.

A diszperzió-kompenzálás az impulzusok Fourier transzformációs határon túli kompresszióját nem teszi lehetővé. Ilyen célból az impulzus spektrumának kiszélesítésére van szükség, amely például az optikai szálakban előidézhető nemlinearitás révén valósítható meg. Alacsony csúcsteljesítmény esetén ez elérhető kis magátmérőjű fotonikus kristály szálakban. Az impulzus terjedésre vonatkozó szimulációnak és optimalizácónak megfelelően, kísérletileg megvalósítottuk a titán-zafír lézer közel transzformáció-limitált 24 fs-os impulzusainak kompresszióját [T2].